Supplementary Material:
Assessing photodamage in live-cell STED microscopy

Nicole Kilian[1+], Alexander Goryaynov[1+], Mark D. Lessard[1], Giles Hooker[2,3], Derek Toomre,[1,4], James E. Rothman[1,4], Joerg Bewersdorf[1,4,5]*

[1]Department of Cell Biology, Yale School of Medicine, New Haven, CT, USA.
[2]Department of Biological Statistics and Computational Biology, Cornell University, Ithaca, NY, USA.
[3]Department of Statistical Science, Cornell University, Ithaca, NY, USA.
[4]Nanobiology Institute, Yale University, West Haven, CT, USA.
[5]Department of Biomedical Engineering, Yale University, New Haven, CT, USA.

+Both authors contributed equally to this work

*Correspondence and requests for materials should be addressed to joerg.bewersdorf@yale.edu.

Supplementary Methods

Next to the description below, detailed information on experimental design and reagents can be found in the **Life Sciences Reporting Summary** accompanying this Correspondence.

Microscopes

We used a Leica TCS SP8 STED 3X (Leica Microsystems GmbH; Wetzlar, Germany), a Leica TCS SP5 STED (Leica Microsystems GmbH; Wetzlar, Germany), a custom-built STED microscope in our laboratory[1] and a LCV110 VivaView Incubator Microscope (Olympus Corp.; Tokyo, Japan) for this study.

Laser Power Measurements

Laser powers on the Leica TCS SP5 STED and custom-built STED microscope were measured using a S130A (Thorlabs, Inc.) photodiode power sensor for the excitation lasers and a S310C (Thorlabs, Inc.) thermal power sensor for the STED lasers in the back aperture plane of the objective. Laser powers on the Leica TCS SP8 STED 3X were measured using a S170C (Thorlabs, Inc.) slide power meter sensor at the position of the microscope sample.

Plasmids and Molecular Cloning

The pSNAPf Vector (N9183S) and the pSNAPf-H2B Control Plasmid (N9186, discontinued in 2015) were both purchased from New England BioLabs, Inc. The plasmids expressing SNAP-tagged OMP25 (SNAP-OMP25) and SNAP-tagged Sec61β (SNAP-Sec61β) were previously described[1]. To generate the plasmid for ManII-SNAP, *Man2a1* was amplified with the following oligos: ManII-sense 5'-atcatcgaattcatgaagttaagtcgccagttc-3' and ManII-antisense 5'-tctgtggaggacggcccgcggtctagacatcat-3' and cloned into a pC4 plasmid using EcoRI and XbaI restriction sites. *MGMT* was cloned with the following oligos: SNAP-tag+Myc-sense 5'-atcatctctagagaacaaaaacttatttctgaagaagatctggacaaagactgcgaaatg-3' and SNAPtag-antisense 5'-atgatgggattcttaacccagcccaggctccgc-3' using XbaI and BamHI restriction sites, respectively.

Preparation of plasmid DNA

The plasmid DNA was prepared from overnight *Escherichia coli*-cultures expressing the above-mentioned plasmids using the QIAGEN Plasmid Maxi Kit (QIAGEN) according to the manufacturer's instructions. DNA concentrations were determined with the NanoVue Plus Spectrophotometer (GE Healthcare).

Cell culture

ATCC CCL-2 HeLa (HeLa) cells and COS-7 ATCC CRL-1651 monkey fibroblast-like kidney cells (COS7) were purchased from ATCC. The cell lines were either maintained in 75-cm^2 rectangular straight neck cell culture flasks with vented cap or in 100-mm tissue culture-treated cell culture dishes (Falcon, Corning Inc.) in a Hera Cell 150 (Thermo Fisher Scientific) or in a Forma Steri-Cult 200 (Thermo Fisher Scientific) incubator at 37°C and 5% CO_2. The cell lines were grown in DMEM (Gibco, Thermo Fisher Scientific) supplemented with 10% heat-inactivated fetal bovine serum (HI-FBS) (Gibco, Thermo Fisher Scientific) as well as 100 units/ml penicillin and 100 µg/ml streptomycin (Gibco, Thermo Fisher Scientific). Optionally, as done in **Supplementary Fig. SN2.1**, **Supplementary Note 5-9**, the growth medium was supplemented with 5% non-essential amino acids (Gibco, Thermo Fisher Scientific), 5% sodium pyruvate (Gibco, Thermo Fisher Scientific) and 100 µg/ml Primocin (InvivoGen).

Preparation of MatTek dishes

For our imaging experiments, we seeded the COS7 and HeLa cells on MatTek 3.5-cm diameter (No. 1.5) glass-bottom dishes (MatTek corporation). The MatTek dishes were cleaned with 1 M KOH (MilliporeSigma) for 15 min in a CPX2800H 0.75 Gallon Ultrasonic Cleaner CPX-952-218R (Branson), sterilized with 70% ethanol and, after several washes with PBS (pH 7.4; Gibco, Thermo Fisher Scientific), coated with fibronectin 1:200 (Hu Plasma Fibronectin, FC010, 1 mg/ml EMD MilliporeSigma) in PBS for 30 min in the incubator at 37°C and 5% CO_2. After additional washes with PBS, the cells were seeded in the freshly prepared MatTek dishes. Unused fibronectin-coated MatTek dishes were filled with PBS and stored in the incubator at 37°C and 5% CO_2 until used (maximum storage time: 1 week).

Transient transfection of cells

HeLa and COS7 cells (~1×10^6 cells per cuvette) were transiently transfected with 5 µg of plasmid DNA via electroporation (Nepa21 Type II, NepaGene Co., Ltd.) following the manufacturer's instructions for adherent cells. The electroporated cells of one electroporation cuvette (0.2-cm gap, NepaGene Co., Ltd.) were evenly distributed on two KOH-cleaned and fibronectin-coated MatTek dishes (see above) and further processed about 16-24 h after transfection.

Generation of stable cell lines

HeLa and COS7 cells were transiently transfected with 5 µg of the plasmid DNA encoding for SNAP-Sec61β. The growth medium was supplemented with G418 Geneticin (Thermo Fisher Scientific) according to the manufacturer's instructions to select for positive clones.

Stocks were prepared from one isolated positive clone. Stably transfected cells were not passaged more than 10 times.

Drug Control Experiments

The following drugs were used for Ca^{2+}-release control experiments: Ionomycin (IO) (Santa Cruz Biotechnology), Thapsigargin (TG) (Sigma-Aldrich) and AntimycinA (AntA) (Enzo Life Sciences, Inc.). Stock solutions of Ionomycin, Thapsigargin, and Antimycin were diluted in imaging buffers (buffers described below) to achieve the following concentrations: 2 µM Thapsigargin, 5 µM Ionomycin and 10 mM Antimycin A. The drugs were added to the cells on the microscope stage within the first 10-15 s of imaging and the Ca^{2+}-response of the cells was monitored for about 10 min. Data for each data set was acquired on three different days.

ROS (reactive oxygen species) scavenging buffer experiments

The ROS scavenging buffer is a solution of ascorbic acid (1 mM; BioVision Inc.), catalase (250 units/ml; MP Biomedicals, Inc.; 100429; lot number Q5405), pyranose oxidase (7.5 units/ml; Sigma-Aldrich; P4234-250UN; lot numbers SLBQ1525V, SLBT6425), the α-tocopherol analogue Trolox (1 mM; VectaCell Trolox Antifade, Vector Laboratories) and TEMPOL (500 µM; Enzo Life Sciences, Inc.; ALX-430-081-G001; lot number 01101705)[2,3]. The buffer was freshly prepared for every imaging experiment. The components were dissolved in Live Cell Imaging Solution (Thermo Fisher Scientific), with addition of 20 mM α-D-glucose (Sigma-Aldrich) and 20 mM Tris:HCl pH 7.4 (Sigma-Aldrich). For our Ca^{2+}-response experiments, cells were first labeled with FluoForte (see below). ROS scavenging buffer was only added after the incubation with FluoForte was completed. We replaced the FluoForte dye loading solution with the ROS scavenging buffer (supplemented with Reagent A (FluoForte dye)) without washing the cells. A positive control with 5 µM Ionomycin was further conducted to ensure that the cells were still able to show a Ca^{2+}-response even when they were maintained in ROS scavenging buffer. In early FluoForte experiments (**Supplementary Fig. SN5.1c**), HEPES (Thermo Fisher Scientific) and HBSS (Hanks Balanced Salt Solution) (Thermo Fisher Scientific) with the addition of 20 mM α-D-glucose (Sigma-Aldrich) was used instead of Live Cell Imaging Solution.

Labeling of live cells for irradiation experiments

The following fluorescent dyes were used for irradiation experiments: FluoForte (FluoForte-AM, acetoxymethyl ester) (ENZ-51017, Enzo Life Sciences, Inc., lot numbers 11081713, 04181723) and GFP-certified FluoForte (ENZ-52016, Enzo Life Sciences, Inc.); SNAP-Cell 647-SiR (SiR-BG, silicone rhodamine-benzylguanine) (S9102S, New England BioLabs, Inc.). Cells were labeled for 1 h with 5 µM of SNAP-Cell 647-SiR (1 mM stock solution in DMSO (dimethyl sulfoxide); Invitrogen) 16-24 h after transient

transfection of the plasmids encoding for the above described SNAP-tagged proteins[4]. Afterwards, the cells were extensively washed with growth medium and kept for about 1-3 h at 37°C and 5% CO_2 to allow the excess dye to leave the cells. Once the labeling with SNAP-Cell 647-SiR was completed, the cells were washed 3 times with PBS and treated with FluoForte following the manufacturer's recommended protocol. For the FluoForte experiments shown in **Fig. 1**, **Supplementary Fig. SN3.1** and **Supplementary Fig. SN11.1**, we used Live Cell Imaging Solution (Thermo Fisher Scientific) supplemented with 20 mM Glucose, dye efflux inhibitor (Reagent B) and the FluoForte dye (Reagent A) as FluoForte dye loading solution. For the experiments described in **Supplementary Notes 2** and **5-9** we used the manufacturer's suggested FluoForte dye loading solution.

STED imaging on Leica TCS SP8 STED 3X

The STED irradiation results presented in **Fig. 1** (or **Supplementary Fig. SN4.1**), **Supplementary Fig. SN2.2**, **3**, **4**, **10** and **11** were acquired with a Leica TCS SP8 STED 3X microscope (Leica Microsystems) equipped with a live-cell imaging chamber (37°C, 5% CO_2; Stage Top Incubator, Tokai Hit) and a Leica HC PL APO CS2 100x/1.40 oil immersion objective. SNAP-Cell 647-SiR was excited at 640 nm (~38-59 µW). A pulsed 775-nm laser (~80 mW-143 mW) was used for depletion of SNAP-Cell 647-SiR. A HyD detector with the detection window set to 650-700 nm was used for detection. The pinhole was set to 1 AU. The cell of interest was selected based on general morphology and SNAP-Sec61β expression level. The typical STED irradiation series (1024 x 1024 pixels, image size 58 µm x 58 µm) was acquired in STED mode using the 8-kHz scanner repeating an about 12-s long 9-frame imaging cycle for about 10 min. The FluoForte signal was imaged in the first frame of each imaging cycle with the 488-nm laser (HyD detector with detection window 500-550 nm) at minimal laser power (~2.4 µW) to minimize FluoForte bleaching and avoid unnecessary irradiation with blue light. The 640-nm and 775-nm lasers were turned on during all frames of each imaging cycle. Scanning at 8-kHz line scan frequency with bidirectional exposure and 16x line averaging resulted in a pixel dwell time of ~0.58 µs per frame and a total time per frame of ~1 s.
For the negative control experiments shown in **Fig. 1a** and **Supplementary Fig. SN2.2a**, we used the same parameters, but switched off the 640-nm and the 775-nm laser to avoid excitation of SiR-BG. The Ionomycin experiments presented in **Fig. 1b**, **Supplementary Fig. SN2.2b** and **Supplementary Fig. SN3.1** were recorded with the same microscope settings as described for the negative control experiments. However, we used a Leica HC PL APO CS 10x/0.40 dry objective (1024 x 1024 pixels, image size 930 µm x 930 µm) to avoid analysis artifacts from cells moving out of focus when adding Ionomycin.
The overview images for **Fig. 1e,f,i,j** (or **Supplementary Fig. SN4.1a,b,e,f**) (1024 x 1024 pixels, image size 58 µm x 58 µm) were acquired in confocal and brightfield mode with a 8-kHz resonant scanner using 64x line averaging and unidirectional scan mode. The short imaging series shown in **Fig. 1g,h,k,l** (or **Supplementary Fig. SN4.1c,d,g,h** (1024 x 1024 pixels, image size 19.4 µm x 19.4 µm) were acquired in STED mode using the 8-kHz scanner, 256x line averaging and bidirectional scan mode.
Supplementary Video 1 was acquired in STED mode as described above (1024 x 1024 pixels, image size 19.4 µm x 19.4 µm) with the 8-kHz scanner using 16x line averaging

with bidirectional scan (0.58 µs pixel dwell time, ~1 fps) without FluoForte labeling and excitation.
To measure photobleaching (**Supplementary Fig. SN4.2**), we imaged cells in STED mode (1024 x 1024 pixels, image size 58 µm x 58 µm, 0.58 µs pixel dwell time, ~1 frame/s) without acquiring FluoForte images (see above). Data for each data set, except for the photobleaching experiment, was acquired on three different days.

STED imaging on the Leica TCS SP5 STED

Data presented in **Supplementary Fig. SN2.1** and **Supplementary Fig. SN5.1-9** were acquired with a commercial Leica TCS SP5 STED microscope using a 1-kHz scanner and equipped with a 100X/1.4 NA oil immersion objective lens and a live-cell imaging chamber (37°C; The Box, Life Imaging Services). A 488-nm, 530-nm and pulsed 635-nm laser were used to excite FluoForte, GFP-certified FluoForte and SNAP-Cell 647-SiR, respectively. A pulsed 770-nm laser was used for the depletion of SNAP-Cell 647-SiR. Fluorescence was detected using avalanche photodiodes. Photodamage induced by shorter wavelengths (**Supplementary Fig. SN9.1**) was tested with a 458-nm laser light (11 µW). In this case, the red-shifted GFP-certified FluoForte was used instead of FluoForte. The emitted fluorescence from FluoForte and GFP-certified FluoForte was collected in the wavelength range of 505-530 nm, and 530-570 nm, respectively. The pinhole size was set to 2 AU. The imaging experiments were conducted as follows: a single cell was selected by first having a quick look at the general morphology in DIC (differential interference contrast) and then at the expression levels of the SNAP-tagged proteins in the 635-nm channel. The field of view was normally selected to be ~50 µm x 50 µm (1024 x 1024 pixels, ~50 nm pixel size). Then, the cell was imaged in sequential mode with one image taken with the 488-nm laser (or 530-nm laser for red-shifted GFP-certified FluoForte) every 10 s at minimal laser power of 0.2 µW (the minimum that allowed to collect reasonable signal from FluoForte, avoiding unnecessary irradiation). The 635-nm (~20 µW) and 770-nm lasers (~40 mW) were constantly scanning the sample at 1-kHz line scan frequency (unidirectional exposure), resulting in a pixel dwell time of about 0.4 µs per frame, recording about 1 frame/s, for 600 s. Data for each data set was acquired on three different days.

STED imaging on custom-built STED microscope

A custom-built STED instrument[1] was used for experiments at 16-kHz line scan frequency (**Supplementary Fig. SN5.1b,c**). The microscope was equipped with a live-cell imaging chamber (37°C, 5% CO_2) (Okolab). Previously used imaging conditions and parameters[1] were replicated for the excitation of SNAP-Cell 647-SiR using a 650-nm excitation laser (~20 µW) and a 775-nm STED laser (~140 mW)[1]. Similar to the experiments on the Leica SP5 and SP8 instruments, additionally, one image of the FluoForte fluorescence was acquired every 10 s with a 485-nm laser at a minimal laser power of 5 µW. The field of view was 25.6 µm x 25.6 µm (512 x 512 pixels). Using 32 line averages and unidirectional

exposure, this resulted in a pixel dwell time of about 1.3 µs and a recording speed of about 1 frame/s. Data for each data set was acquired on three different days.

Long-term viability imaging after STED irradiation

COS7 and HeLa cells were transfected with SNAP-Sec61β and seeded on a KOH-cleaned and Fibronectin-coated gridded MatTek dish (P35G-1.5-14-C-GRID), labeled with SiR-BG, incubated with Live Cell Imaging Solution (Thermo Fisher Scientific) supplemented with 20 mM Glucose, dye efflux inhibitor (Reagent B) and the FluoForte dye (Reagent A). After noting their position on the grid, individual cells were STED-irradiated for ~10 min with the Leica TCS SP8 STED 3X as described above. These irradiation experiments were conducted sequentially on five cells per MatTek dish. Afterwards, the cells were washed multiple times with DMEM (without phenol red, supplemented with 10% FBS) and kept in this buffer for the remainder of this experiment. Two MatTek dishes were imaged per session (one HeLa, one COS7 dish). The first one was kept in an incubator (37°C, 5% CO_2) after irradiation experiments while the second dish was irradiated. After completion of the irradiation experiments, both dishes were transferred to a long-term imaging incubator microscope system (LCV110 VivaView, Olympus; located in a different building). The grid areas of the ten STED-irradiated cells (five in each dish) were identified on this microscope and DIC images of the designated areas were recorded every 15 min for 24 h. These experiments were conducted on three different days, resulting in 15 cells per cell line.
By visually examining the videos, the cell fate was determined. However, not every STED-irradiated cell could be identified with absolute certainty since some cells had moved substantially during the 0.5-6 h gap between irradiation experiments and the beginning of the video sequences. To avoid a selection bias for either dead or surviving cells in the analysis, instead of dropping these data sets from the analysis, we decided to introduce a third category of 'indeterminable' fate (labeled with a "?" in **Fig. 1m**) next to 'dead' and 'alive' categories. As negative controls we randomly selected one to two healthy-looking cells in each field of view recorded by the VivaView instrument, about three to ten cell diameters away from the STED-irradiated cell and well outside the STED irradiation field, from the first frame of each video and determined their cell fate. Since the control cells did not need to be matched to STED-irradiated cells, the 'indeterminable' category did not apply here. **Supplementary Videos 2** and **3** show examples of STED-irradiated COS7 cells in the 'alive' and 'dead' category, respectively.

Image processing and quantification

Raw images were analyzed and prepared for presentation using Fiji (imagej.net/Fiji). For the quantifications presented in **Fig. 1**, **Supplementary Fig. SN2.2**, **Supplementary Fig. SN3.1** and **Supplementary Fig. SN11.1**, three 5x5-μm^2 large ROIs (regions of interest) were drawn at random locations on the FluoForte-labeled cells. Three additional ROIs of the same size were drawn outside the cells to estimate the background. The integrated density was determined using the Time Series Analyzer V3 plugin. The mean integrated

density of the three background squares was subtracted from the mean integrated density of the three squares drawn on the cell to generate a damage response curve for each recorded cell. Each curve was further normalized to its value at the first time point.
SiR-BG bleaching curves (**Supplementary Fig. SN4.2**) were acquired in the same way but using the SiR instead of the FluoForte signal. The half-life was determined fitting a single exponential decay function using GraphPad Prism 7.0a.
For the quantifications presented in **Supplementary Fig. SN2.1** and **Supplementary Note 5-9**, the cells were outlined and the average intensity in the outlined regions was measured with the background subtracted to acquire damage response curves. Matlab was used to determine average height, width and location of the FluoForte peaks. The curves were further normalized to their value at the first time point and plotted in the same graph for comparison.

Determination of STED video resolution

A recently developed Nested-loop Ensemble PSF (NEP) fitting technique was used to determine the resolution of the STED videos. See Barentine *et al*.[5] for further reference. Resolution estimates are summarized in **Supplementary Note 10**.

Statistical analysis

We define as "independent experiments", experiments performed on different days.

All analyses were conducted in the R statistical programing language (www.r-project.org). The maximum of each response curve and its value at 10 minutes were screened for batch effects of technical replicates within each experimental condition separately (R function aov). With no significant effects reported, pairwise comparisons were made between negative control, STED, and ROS buffer treatments in each of the COS7 and HeLa cell lines separately. These comparisons were based on the proportion of cells with maximum response greater than 2 and conducted using Fisher's exact test (R function fisher.test). Positive controls were significantly different from all other conditions in both cell types ($p<0.003$ in all cases) while no significant differences were observed between the three remaining groups ($p>0.2$). See table below.

Comparison	**Cell Line**	**Stressed/Total Cells**	**p-value (Fisher's Exact Test)**
STED vs Neg Control	COS7	0/30 vs 0/18	1
	HeLa	3/30 vs 0/17	0.29
Neg vs Pos Control	COS7	0/18 vs 15/15	1e-9
	HeLa	0/17 vs 15/15	1e-9
STED vs Pos Control	COS7	0/30 vs 15/15	3e-12
	HeLa	3/30 vs 15/15	7e-10
STED vs ROS	COS7	0/30 vs 0/30	1
	HeLa	3/30 vs 0/32	0.24

For long-term viability studies, pairwise comparisons within each cell line of the number surviving were conducted to compare control and STED-imaged cells based on Fisher's exact test. We considered three different scenarios for the interpretation of cells with indeterminable fate to address sensitivity to the missingness mechanisms: (1) ignoring them in the statistical analysis, (2) assuming that they were all alive, (3) assuming that they were all dead. In scenario (1), pairwise comparison showed marginally significant differences for COS7 cells (4/9 STED, 22/28 control, p=0.091), and significant differences for HeLa (4/12 STED, 16/20 control, p=0.021). Scenario (2) resulted in no statistically significant difference for COS7 cells (10/15 STED, 22/28 control, p=0.473) and a marginal statistical difference for HeLa cells (7/15 STED, 16/20 control, p=0.0713). Scenario (3) resulted in statistically significant differences for both COS7 and HeLa cells (4/15 STED, 22/28 control, p=0.0025 and 4/15 STED, 16/20 control, p=0.0024, respectively). In all cases a lower percentage of STED-imaged cells survived than in the control condition.

Code availability statement

The used Matlab and R Code is available from the corresponding author upon reasonable request.

Data availability statement

The authors declare that the data supporting the findings of this study are available from the corresponding author upon reasonable request.

Supplementary Note 1: Ca^{2+} is a viable cell stress indicator

Ca^{2+} plays a crucial role as extra- and intracellular messenger

A variety of short-term and long-term biological processes such as cell regulation, metabolic modulation, myofilament contraction, mitotic division and gene expression are regulated by the change of Ca^{2+} levels inside and outside of the cell[6-11]. As an extracellular messenger, for example, Ca^{2+} controls the gating properties of plasma membrane channels and acts as an agonist for G protein-coupled Ca^{2+}-sensing receptors[12]. As an intracellular second messenger, Ca^{2+} can build up local concentration gradients in the cytoplasm that can amplify themselves[9,13-15]. The resting level of free Ca^{2+} in the cytoplasm is ~0.1 µM, but levels of 1 µM or higher can temporarily be reached as a result of induced signal transduction or insult[16-22].

The cytoplasmic homeostasis of Ca^{2+} is tightly controlled. It is mainly regulated by Ca^{2+} transport through the plasma membrane (PM) or in and out of the endoplasmic reticulum (ER) or, in the case of excitable striated muscle cells, the sarcoplasmic reticulum (SER)[23]. The Ca^{2+} levels in the ER can reach 10-100 mM whereas other organelles such as the mitochondria or the Golgi apparatus contain ~100 µM and 300 µM Ca^{2+}, respectively[6,24-28]. The ER therefore represents the major intracellular Ca^{2+} storage of the cell, whereas mitochondria rather decode, shape and buffer the cellular Ca^{2+} signals by well-defined uptake and release mechanisms that can induce various cell death modalities[25,29].

Ca^{2+} is involved in several cell-death modalities

Cell death can be classified according to its morphological appearance, enzymological criteria, functional aspects or immunological characteristics[30]. In 2009, the Nomenclature Committee on Cell Death (NCCD) suggested the use of morphological criteria to define cellular catabolism, such as ‘apoptosis’, ‘necrosis’ and ‘autophagy’[31,32]. Substantial progress in discovering the underlying genetic and biochemical mechanisms and patterns led to a switch from morphological to molecular definition of the previously established cell-death modalities three years later[33]. Ca^{2+} is a key initiator and effector in several of the above-mentioned cell-death modalities[22,34-36].

The first identification of Ca^{2+} as an initiator of cell-death dates back to 1974 when Fleckenstein and coworkers observed that excess Ca^{2+} entry into cardiomyocytes leads to ischemia and subsequent cardiac pathology[37]. More recent experimental approaches have established the involvement of Ca^{2+} in apoptosis, necrosis, anoikis, autophagic cell-death and netosis[33,38,39].

In particular:

- The role of Ca^{2+} in autophagy and autophagic cell-death is still not very well understood, but oxidative stress-triggered autophagic cell death appears to be apoptosis-independent[40]. Lysosomal calcium signaling seems to regulate calcineurin and to induce autophagy[41]. Ca^{2+}-permeable channels are also potential candidates for autophagy regulation[42].
- In the case of an intrinsic stress signal, caspase-dependent and caspase–independent pathways can be activated[33,38]. Ca^{2+} regulates the caspase-dependent pathway but can also play a role in the caspase-independent pathway[35,43,44].

The role of Ca^{2+} in apoptosis and necrosis

The ER stores the majority of intracellular Ca^{2+} for signaling purposes as well as for folding and modifying newly synthetized proteins[29,45]. The disturbance of one of these functions or any damage to the ER can cause the depletion of luminal Ca^{2+} and ER stress[46,47]. This initial release of Ca^{2+} can be channeled into nearby mitochondria via reversibly tethered mitochondria-associated membranes (MAM) or other processes[13,36,48-53].

Mitochondria act as a node for intracellular Ca^{2+} communication since the organelles require a specific concentration range of the constitutively ER-released Ca^{2+} for their respiration and ATP production processes[54]. An increase of the cytosolic Ca^{2+} concentration beyond a threshold of ~500 nM automatically triggers mitochondrial participation since the organelles possess low affinity (500 nM) Ca^{2+} uniporters (mCU) that facilitate the uptake and storage of the Ca^{2+} in the mitochondrial matrix (Ca^{2+}mt)[55,56]. Ca^{2+} that has been stored in mitochondria can be released again to help refill the luminal

Ca^{2+} stocks of the ER after signal transduction-induced depletion or until a Ca^{2+} stress situation has resolved[8,57,58].

If the amount of sequestered Ca^{2+} exceeds the capacity of the mitochondria, the multi-ion mitochondrial permeability transition pores (mPTPs) open and Ca^{2+} is dissipated from the mitochondrial matrix into the cytoplasm causing adjacent unaffected mitochondria to respond to the concentration-increase by taking up Ca^{2+} as well[25,59,60]. This can lead to a mitochondrial suicide cascade, which will result in the demise of the cell due to cytochrome c release via mPTP opening[60,61]. The release of cytochrome c, despite the lack of an upstream apoptotic signal like Bax (Bcl-2 (B-cell lymphoma 2)-associated X protein) translocation, can still activate the caspase cascade and turn an apparent initial necrotic cell-death into a physio-compatible apoptosis[60]. Minor release episodes of cytochrome c as a result of changes in Ca^{2+} levels further suggest that small amounts might already be sufficient to initiate apoptotic pathways since cytochrome c can induce further conductance of Ca^{2+} through the inositol triphosphate receptors (InsP3Rs) in the ER membrane[48]. The resulting mass-release of cytochrome c engages the cytoplasmic protein Apaf1 (Apoptotic protease activating factor 1) to form the apoptosome and to activate caspase-9 dimerization, which will trigger an autocatalytic process that results in further biochemical and structural changes such as pyknosis, cytoplasmic shrinkage, nuclear fragmentation and blebbing of the PM[6,48]. At the end of the apoptotic process, the cell breaks down into multiple encapsulated fragments (apoptotic bodies), which are finally devoured by tissue macrophages and neighboring tissue cells[6,48].

Both apoptotic and necrotic pathways are under given circumstances able to cooperate via a balanced interplay that additionally involves autophagy, or are applied in a complementary way[62].

Necrosis has initially been regarded as the result of an accidental and uncontrolled cell event that is caused by external factors such as infection, toxins, heat or trauma, which can lead to a severe Ca^{2+} dysregulation causing the release of cytoplasmic material and a subsequent inflammatory reaction[44,63]. One common cause of necrosis is the collapse of mitochondrial energy metabolism leading to an increase of the intracellular Ca^{2+} concentration and the subsequent stimulation of various Ca^{2+}-dependent catabolic enzymes such as phospholipases, proteases and endonucleases[22,34,64]. The necrotic process leads to

the disruption of the plasma membrane, cell swelling, chromatin condensation and cell lysis[22,65]. It has further been discovered that the process can also be mediated by a specific set of signal transduction pathways and degradative mechanisms[31]. In recent years multiple cell-death modalities have been assigned to regulated necrosis, such as necroptosis, parthanatos, ferroptosis or oxytosis, mitochondrial permeability transition (mPT)-dependent necrosis, pyroptosis and pyronecrosis, as well as cell death associated with the release of (neutrophil) extracellular traps commonly known as NETosis or ETosis[66].

Due to its involvement in many cell-death-associated processes, Ca^{2+} is a viable indicator to monitor cell health and cell viability[52,67].

Ca^{2+} release can be triggered by light via reactive oxygen species

Multiple studies have shown that light irradiation in a wide spectrum (360-490 nm and 500-635 nm as well as 780 nm) is able to trigger Ca^{2+} influx into the cell, Ca^{2+} release from the ER as well as further Ca^{2+} uptake or overload in mitochondria due to dye-specific reactive oxygen species (ROS) stress that was generated during the imaging experiment[15,68-75]. ROS such as hydrogen peroxide (H_2O_2), superoxide and singlet oxygen are derived from molecular oxygen in various subcellular compartments including mitochondria, ER, several enzyme systems within the cytoplasm and at the plasma membrane[76,77,78,79].

Years of research have further revealed that ROS are more than an unwanted waste product of certain metabolic reactions within the cell, but important signaling factors in multiple physiological processes[76,80]. However, there is a fine balance between the generation and the scavenging of ROS since excess production causes cell damage via disruption of membranes, and protein and DNA structures[81].

Increasing evidence further suggests a tight interaction between ROS and Ca^{2+} signaling pathways[77,78]. Ca^{2+} and ROS are considered main factors, which can partially propagate and execute necrosis and further apoptosis by direct or indirect provocation of DNA, lipid and protein damage[28,34,77].

During imaging experiments, an excess of ROS can be generated by fluorophores[82]. Any labeling dye that is applied in a nanoscopic imaging experiment should therefore be considered a photosensitizer that might be able to damage subcellular structures by

triggering Ca^{2+} release due to the connection of ROS and Ca^{2+} signaling systems[77,78,83]. Monitoring the Ca^{2+} concentration in the examined cell can therefore indicate whether photodamage has taken place during the imaging experiment and further determine the severity of the damage.

Ca^{2+} is a valuable indicator of photodamage for imaging experiments

It has been notoriously difficult to establish general photodamage criteria based on cellular structure or functional assays that allow to reliably quantify damage in real time while the experiment is being conducted[82]. Cell populations often show highly heterogeneous behavior during the imaging experiment, which is difficult to interpret[84]. Therefore, many previously conducted studies on photodamage focused on extreme characteristics such as the fraction of dead cells, mitotic arrest, DNA defects, cytoskeletal defects or developmental defects in various organisms such as *Caenorhabditis elegans* and *Drosophila melanogaster* as indicators of irreversible cell damage after light irradiation[48,82,85-88]. Further components that were considered to be potential indicators for cell stress were nitric oxide (NO), various ROS and the microtubule-associated protein 1A/1B-light chain 3 (LC3)[89-95]. However, none of the mentioned components are ideal to be used as indicators since they are not generally applicable or their readout is not sensitive enough to detect early signs of cell stress.

It has been shown previously that the imaging process can generate waves of free Ca^{2+} in the cytoplasm of various cell types[7,13,21,48,52,96-101]. Combined with its central and early role in multiple cell stress signaling pathways outlined above and relatively easy means to monitor its cytoplasmic concentrations, we therefore chose increases of free Ca^{2+} levels as a robust and sensitive indicator of light-induced cell stress.

Supplementary Note 2: FluoForte is a sensitive detector of cytoplasmic Ca^{2+} changes

To test for changes in the Ca^{2+} concentration during image acquisition, a highly sensitive and non-toxic compound must be used. This compound ideally needs minimal sample preparation and is easily applicable. We chose FluoForte (Enzo Life Sciences Inc.) because it is cell permeable, non-toxic, bright and requires only minimal sample preparation, which helps to reduce pre-imaging stress for the cells[102,103].

FluoForte has previously been applied to monitor intracellular Ca^{2+} levels in a range of specimens using different microscopy approaches. For example, Rivas-Sendra *et al.* imaged Ca^{2+} dynamics in living rapeseed (*B. napus*) and eggplant (*S. melongena*) microspores and pollen grains during development with a confocal laser scanning microscope[104]; Song *et al.* examined Ca^{2+} handling in induced pluripotent stem cell models of cardiac arrhythmias with an epifluorescent widefield microscope[105]; Crocini *et al.* monitored local alterations of Ca^{2+} release in heart failure using random access multiphoton microscopy[106].

The fact that FluoForte can detect intracellular Ca^{2+} changes in various specimens with different microscopes speaks to its general applicability. Combined with our own experiences of its application in STED microscopy (see below), we believe that it can be a useful assay also for other super-resolution techniques in the future.

FluoForte and cell stress

As discussed in **Supplementary Note 1**, excess cytoplasmic Ca^{2+} concentrations are able to trigger several cell death modalities[22]. Free cytoplasmic Ca^{2+} concentrations of ~1 µM can be considered the maximum tolerable amount of unbound Ca^{2+}[22]. Based on the estimated K_d of FluoForte (389 nM) (http://www.axxora.com/support/dyes-cellular-analysis/cellestial-dyes-kits-faqs/) and our Ionomycin control (see **Fig. 1b** and description below), we defined a conservative damage threshold regarding FluoForte signal increase (F/F_0): F/F_0 ratios below 2.0 were regarded as synonymous for low levels of Ca^{2+} increase (below roughly 300 nM) that correspond to tolerable phototoxic impact. Levels above 2.0 are considered to be problematic.

As control for our FluoForte assay in our chosen mammalian cell systems COS7 and HeLa, we measured the FluoForte response to Ionomycin (IO) as well as Thapsigargin (TG) and Antimycin A (AntA).

We transfected our cells with the *SEC61B* gene encoding for the β-subunit of the ER-localized protein translocon Sec61 (Sec61β) tagged with an engineered version of the *MGMT* gene (also denoted as *AGT*) that encodes for the mammalian enzyme O-6-methylguanine-DNA methyltransferase, which is known and will be referred to as SNAP-tag protein [107-109]. The cells were then labeled with 5 µM SNAP-Cell 647-SiR (SiR-BG, silicone rhodamine-benzylguanine)[1] and further treated with 5 µM Ionomycin.

Ionomycin:

Ionomycin is a diacidic polyether, which was originally isolated from *Streptomyces conglobatos*[110]. IO acts as a selective Ca^{2+} ionophore, which makes cellular membranes highly Ca^{2+} permeable[111-113]. The treatment of HeLa and COS7 cells with 5 µM IO after about 10 s of imaging resulted in a very strong increase of the cytoplasmic Ca^{2+} concentration in both cell lines as indicated by the FluoForte signal (**Fig. 1b**).

Negative Control:

As a negative control, we examined the FluoForte signal in COS7 and HeLa cells treated and labeled in the same way as in the Ionomycin experiment but did not apply IO during image acquisition. Cells in this experiment, as well as in the Ionomycin experiment, were only illuminated by the light required to read out the FluoForte signal as described in the **Supplementary Methods**, but not the SiR excitation and STED lasers. The absence of a FluoForte signal increase in the negative control experiments confirmed that the cell treatment with FluoForte and SiR itself, as well as the transfection and the FluoForte signal measurements on the microscope, did not result in a measurable damage response (**Fig. 1a**).

Additionally to our experiments using a Leica TCS SP8 STED 3X microscope, we performed the above described negative and positive IO control experiments with a Leica TCS SP5 STED microscope where we also observed strong Ca^{2+}-response profiles

(**Supplementary Fig. SN2.1d**). We further used the Leica TCS SP5 STED microscope to examine the Ca^{2+}-response of COS7 and HeLa cells when treated with TG and AntA as additional positive controls.

Thapsigargin:

TG, a sesquiterpene lacton tumor promoter isolated from *Thapsia garganica*, disrupts the cytoplasmic Ca^{2+} homeostasis by the non-competitive inhibition of the sarco/endoplasmic reticulum Ca^{2+}-ATPase (SERCA), which transports Ca^{2+} from the cytoplasm to the ER lumen[114-116]. The treatment of the cells with TG rapidly increases the Ca^{2+} concentration in a dose-dependent manner. It has previously been shown that a final concentration of 2 µM is able to affect SERCA[117-119]. Mitochondria respond to the TG stimulus by a rapid biphasic fragmentation with the initial fragmentation event occurring within minutes depending on the increase of intracellular Ca^{2+} levels and the influx of Ca^{2+} into the organelle[120]. The link between TG-induced increase of the concentration of cytoplasmic Ca^{2+} and the activation of apoptotic pathways has also been observed in different studies that have investigated various cell types[121,122].

HeLa and COS7 cells were treated with TG after about 15 s of imaging. Both cell lines instantly responded to the treatment with TG by releasing Ca^{2+} out of the ER into the cytoplasm as indicated by the FluoForte signal (**Supplementary Fig. SN2.1a**).

Antimycin A:

AntA is a secondary metabolite produced by different *Streptomyces* species[123]. The compound binds to the Q_i site of the cytochrome bc_1 complex (cytochrome c oxireductase or complex III) in the mitochondrial respiratory chain and blocks the oxidation of the cytochrome *b* hemes in the low potential chain[124]. Since the cytochrome bc_1 complex is a crucial enzyme of the oxidative phosphorylation of the mitochondria, its inhibition will eventually cause the disruption of the carefully maintained proton gradient across the inner membrane of the organelle and trigger the production of superoxide[124]. Due to its ability to block the electron transport chain, AntA has also been used to induce chemical hypoxia[125]. The treatment with 10 mM AntA caused a steady increase in Ca^{2+} levels, reaching sustained high levels in 200 s (**Supplementary Fig. SN2.1b**). The measurements of the

FluoForte signal were taken for about 600 s after the initial addition of AntA after about 15 s of initial imaging. Our results confirmed the previously described sustained Ca^{2+} release pattern as a reaction to the treatment with AntA[126].

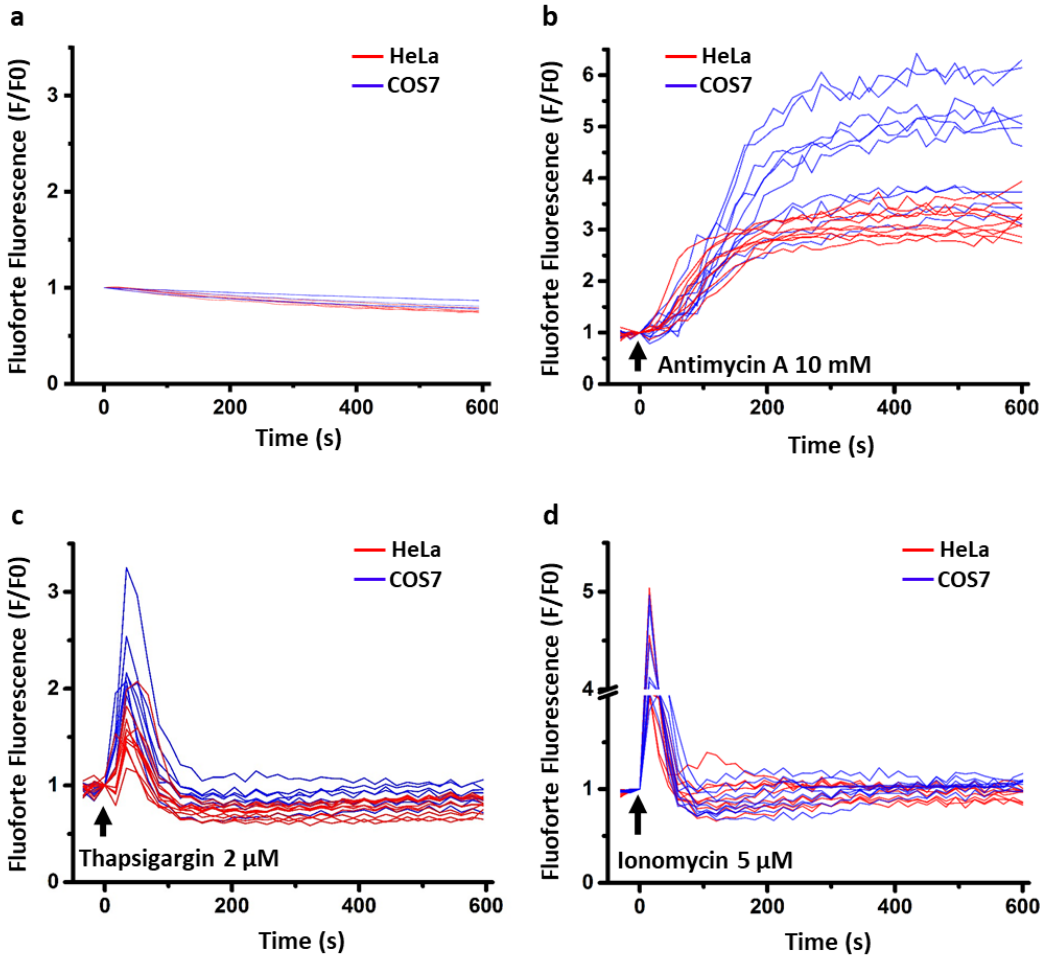

Supplementary Figure SN2.1

Fluoforte shows robust responses to Thapsigargin, Antimycin A and Ionomycin treatment which increase the cytoplasmic Ca^{2+} concentration. HeLa (red) and COS7 (blue) cells were transfected with 5 µg of SNAP-Sec61β plasmid, labeled with 5 µM SiR-BG, incubated with FluoForte and monitored for 10 min. ***(a)*** *Cells showed no measurable cytoplasmic Ca^{2+} level increase under negative control conditions (no red excitation and STED illumination) (HeLa N=5, COS7 N=5).* ***(b-d)*** *Antimycin A, Thapsigargin and Ionomycin were added to the cells after about 15 s of the initial imaging. Antimycin A treatment resulted in a steady increase in cytoplasmic Ca^{2+} with sustained high levels after 200 s of imaging (HeLa N=9, COS7 N=10) (b). Thapsigargin and Ionomycin caused a rapid increase of cytoplasmic Ca^{2+} within seconds after administration (c: HeLa N=10, COS7 N=7; d: HeLa N=9, COS7 N=9) (c,d). A Leica TCS SP5 STED instrument was used for these experiments. Two independent experiments were conducted for (a). Three independent experiments were conducted for (b-d).*

Since our FluoForte control experiments showed a valid response of this Ca^{2+} sensor to intracellular Ca^{2+} changes, we applied FluoForte to examine the Ca^{2+}-response of SNAP-Sec61β-expressing COS7 and HeLa cells during STED irradiation with a 8-kHz resonant scanner (**Fig. 1c**). Only a minor fraction of cells (3 of 30 HeLa cells; 0 of 30 COS7 cells) (**Fig. 1c**) showed a stress response distinguishable from non-STED irradiated cells (not statistically different: HeLa p=0.29, COS7 p=1).

We repeated the above described experiments of **Fig. 1a-c** also with the FluoForte standard buffer (provided by Enzo Life Sciences, Inc.) instead of Live Cell Imaging Solution (**Supplementary Methods**, **Supplementary Fig. SN2.2**). The comparison of the results presented in **Fig. 1a-c** and **Supplementary Fig. SN2.2** shows that both cell lines respond very similarly to IO treatment and STED irradiation, which essentially reproduced our previous observations and further demonstrated that the Live Cell Imaging Solution is an adequate alternative for the company-recommended buffer.

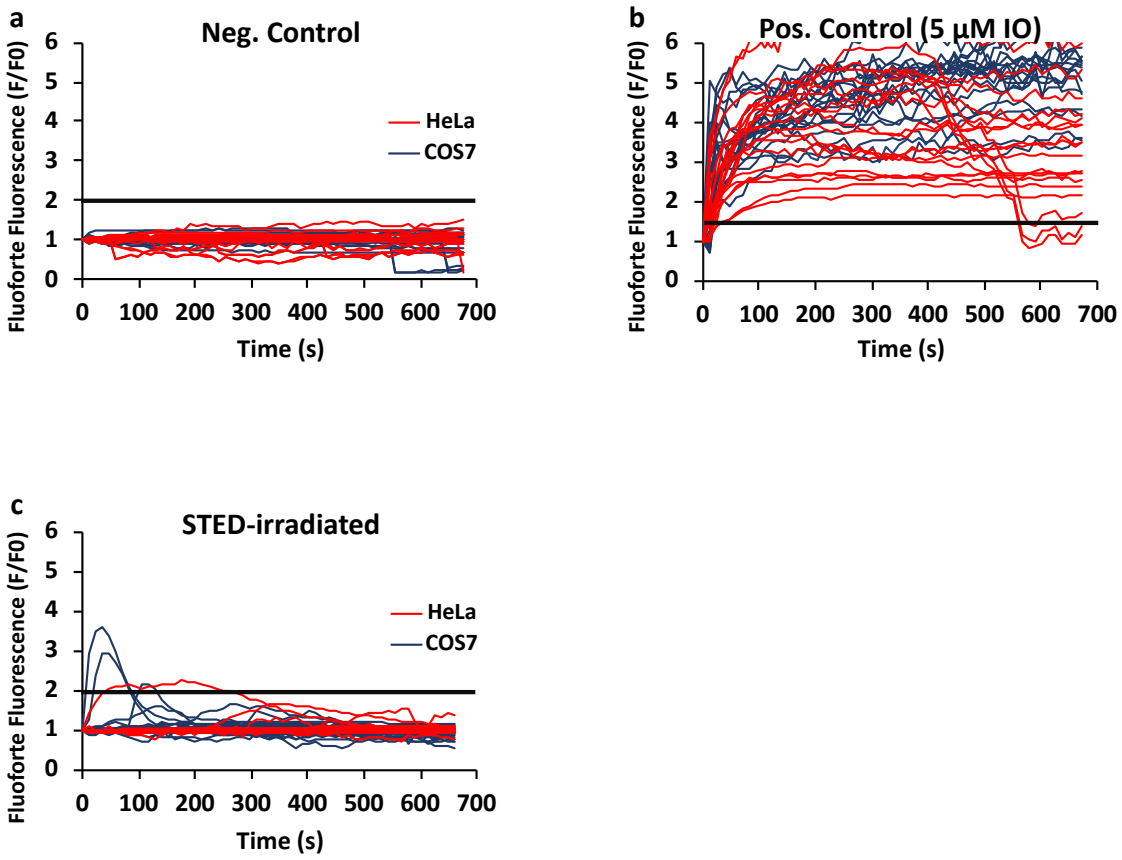

Supplementary Figure SN2.2.

The experiments of Fig. 1 a-c were repeated with FluoForte standard buffer instead of Live Cell Imaging buffer. Comparing the results with Fig. 1 shows that COS7 and HeLa cells respond very similarly to Ionomycin and STED illumination in both buffers, essentially reproducing the findings and demonstrating that the used imaging buffer is an adequate replacement for the company-recommended buffer.

COS7 and HeLa cells transfected with 5 µg SNAP-Sec61β plasmid were labeled with 5 µM SiR-BG, incubated with FluoForte and illuminated for ~11 min. ***(a)*** *HeLa N=17, 4 independent experiments; COS7 N=18, 4 independent experiments;* ***(b)*** *HeLa N=20, 4 independent experiments, COS7 N=20, 4 independent experiments; 5 HeLa cells and 5 COS7 cells were accidently imaged at slightly smaller zoom;* ***(c)*** *STED-irradiation with a fast resonant scanner (8 kHz line scan frequency) caused a response in 3 out of N=30 COS7 cells and 1 out of N=30 HeLa cells.*

Supplementary Note 3: The role of reactive oxygen species (ROS) in photodamage and photobleaching

Photobleaching describes photochemical reaction pathways and undesired photochemical modifications that result in the irreversible loss of a fluorescent molecule's ability to fluoresce[127]. The photobleaching reaction usually originates from the excited triplet state of the fluorophore that is populated via intersystem crossing from the excited electronic singlet state[128]. In contrast to the short-lived (nanosecond) singlet states, the triplet state is usually stable for microseconds to milliseconds[84]. During this time it is vulnerable to further light absorption and reactions that lead to the generation of free chemical radicals such as ROS like the highly reactive singlet form of oxygen as well as the less reactive ground state or triplet form of oxygen, which, however, can be excited to the singlet form[78,82,84,129,79].

The generation of cytotoxic ROS can not only be linked to extrinsic factors like fluorescent probes used for imaging experiments, but also to crucial intrinsic factors like flavins and porphyrins[86,130-134].

A buffer to scavenge ROS

Superoxide anion, hydrogen peroxide or the hydroxyl radical are ROS that can be produced in a cell as a result of an incomplete reduction of oxygen[80] and as a byproduct of the imaging process[82,84,129]. ROS can cause damage to the cell by disrupting membranes, proteins and DNA[82,135,136]. It is further tempting to speculate that the disruption of the membrane of Ca^{2+} storage compartments, such as the ER or to some extend the mitochondria, causes the release of Ca^{2+} into the cytoplasm and the initiation of cell-death modalities[137]. Keeping an appropriate equilibrium between ROS generation and degradation is therefore very important when imaging experiments are conducted. To minimize the production of ROS during STED irradiation, we used a buffer that contained Trolox, ascorbic acid, Tempol and catalase to act as a scavenger for ROS (see **Supplementary Methods**).

Trolox (6-hydroxy-2,5,7,8-tetramethylchroman-2-carboxylic acid) is a water-soluble and cell-permeable analogue of vitamin E[138]. The antioxidant properties of Trolox

are often used in experimental setups, therapies of certain cancers and to avoid cancer predisposition[139,140]. Trolox is further able to suppress the apoptotic program initiated by PDT (photodynamic therapy)[141,142].

Ascorbic acid, or vitamin C, is also a water-soluble antioxidant, which can quench various ROS-mediated signaling events[143,144]. Both ascorbic acid and Trolox have been applied in previous studies that were examining photodamage during microscopic imaging[82,145,146]. The reducing abilities of Trolox and ascorbic acid facilitate the desired repopulation of the singlet ground state of the fluorophore when an oxidant is added as well[147].

We included a membrane-permeable nitroxide and radical scavenger, Tempol (4-hydroxy-2,2,6,6-tetramethylpiperidin-1-oxyl), into our buffer[148,149]. Tempol is able to catalytically dismutate superoxide, facilitate hydrogen peroxide metabolism by using catalase-like actions and further limits the formation of toxic hydroxyl radicals, which are produced by Fenton reactions[149].

The tetrameric catalase is one of the various existing enzymes that catalyze the detoxification of ROS by converting H_2O_2 to water and oxygen without generating further ROS[150].

After transfecting HeLa and COS7 cells with SNAP-Sec61β and labeling the cells with SiR-BG as described above, we imaged the ER of the chosen cells with the Leica TCS SP8 STED 3X (8 kHz line scan speed) for about 10 min while they were maintained in ROS scavenging buffer (**Fig. 1d**).

All cells showed little or no Ca^{2+} response, suggesting that the short-term damaging effects of the given imaging conditions were negligible.

We further tested, if cells would still be able to show a proper Ca^{2+} response in ROS scavenging buffer under positive control conditions by adding 5 µM Ionomycin in the first 10 s of imaging (**Supplementary Fig. SN3.1**). The cells still responded with a strong increase in FluoForte signal.

Although the cells showed little or no response during STED irradiation when kept in the ROS scavenging buffer, the application of this buffer cannot be seen as the ultimate solution for photodamage in every experimental setup. ROS also function as signaling molecules (sROS, signaling reactive oxygen species) that are important for the integrity

(host defense, inflammation and apoptosis) and fitness of organisms and their aging[80,151]. Therefore, we recommend using this buffer only for short-term imaging experiments in the tens-of-minutes range. For longer imaging experiments, it is necessary to determine the various ROS that are generated and to assess their role in cell signaling. Based on this analysis, the appropriate combination of scavengers and their respective concentrations should be individually determined to ensure the health of the cells during the complete imaging process.

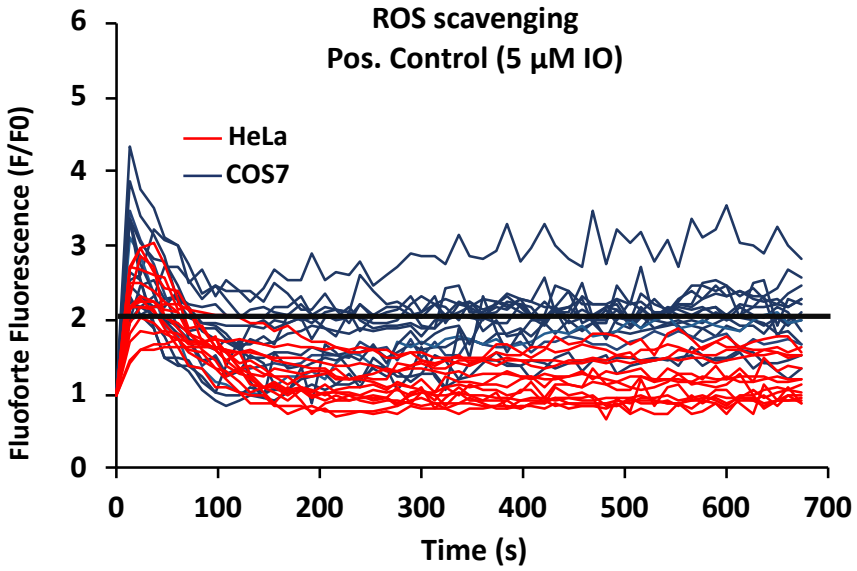

Supplementary Figure SN3.1
COS7 and HeLa cells transfected with 5 µg SNAP-Sec61β plasmid were labeled with 5 µM SiR-BG, incubated with FluoForte and examined in ROS scavenging buffer. A strong increase in FluoForte signal could still be observed when the cells were treated with 5 µM Ionomycin (IO) within 10 s of the initial imaging (HeLa N=15, COS7 N=15). Three independent experiments were conducted for both cell lines.

Supplementary Note 4: Cell morphology and bleaching of the SiR-BG-labeled ER marker Sec61β during STED irradiation

STED imaging of SiR-BG-labeled SNAP-Sec61β allowed us to observe the ER movement in HeLa (**Fig. 1e,l** or **Supplementary Fig. SN4.1** for enlarged and contrast-increased images) as well as COS7 cells (**Supplementary Video 1**) in great detail. There were no suspicious changes visible in cell shape (see corresponding brightfield images **Fig. 1f,j** or **Supplementary Fig. SN4.1b,f**), ER morphology and movement (**Fig. 1g,h,k,l** or **Supplementary Fig. SN4.1c,d,g,h** and **Supplementary Video 1**).

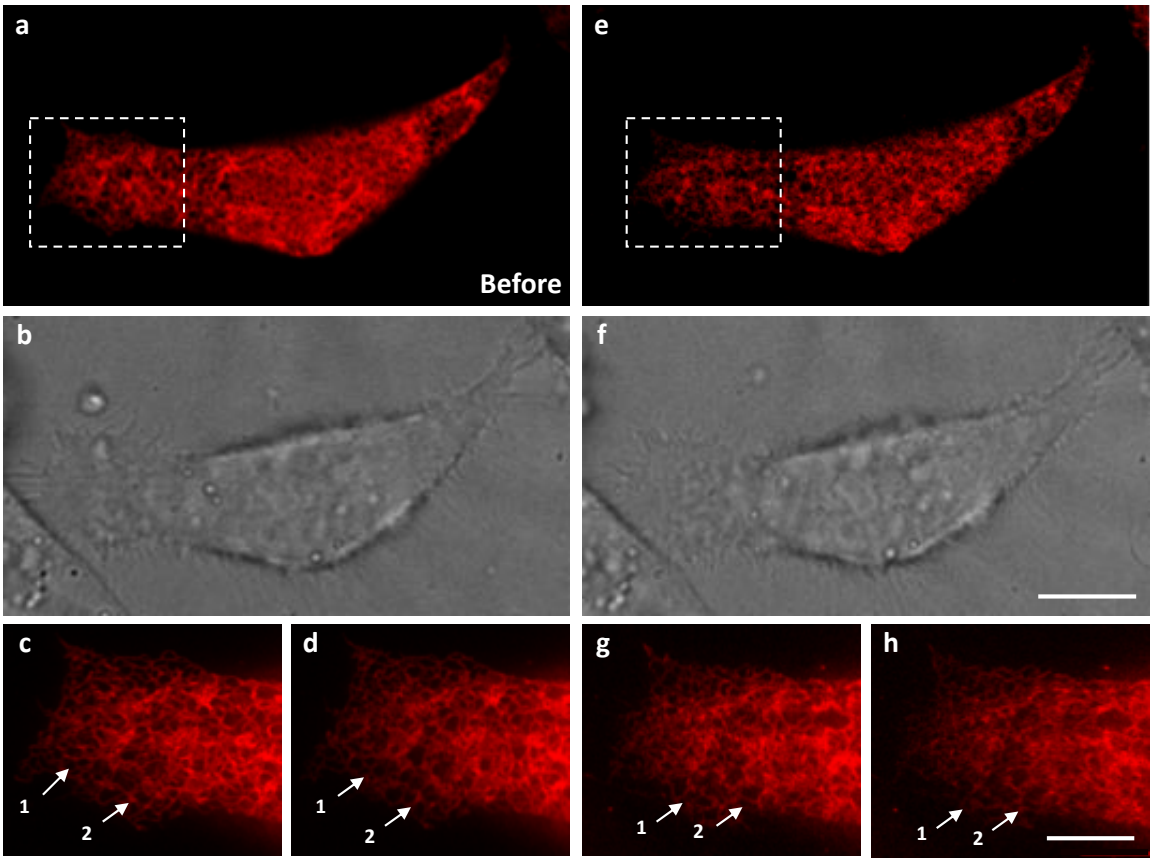

Supplementary Figure SN4.1
Magnified and contrast-increased images of ***Figure 1****. The contrast of the confocal and STED images was adjusted to better show ER structures and movement at the cost of obscuring bleaching and somewhat saturating the images.*

However, as expected in bioimaging applications[152], cells bleached markedly over the course of the imaging experiment. To quantify bleaching, we transiently transfected COS7 and HeLa cells with 5 µg SNAP-Sec61β plasmid, labeled them with 5 µM SiR-BG and imaged them either live (in Live Cell Imaging Solution) or after a 15 min fixation step with 3% PFA and 0.1% GA in PBS. The same imaging parameters were used as for **Fig. 1e,l**. The half-life of the fluorescence loss was determined by plotting the averaged and background-corrected signal for 8 to 9 cells each (**Supplementary Fig. SN4.2**) as described in the **Supplementary Methods**. The fixed cells bleached faster than their live counterparts. The examined fixed COS7 cells bleached the fastest with a half-life of about 119 s, whereas the live HeLa cells bleached the slowest with a half-life of about 194 s.

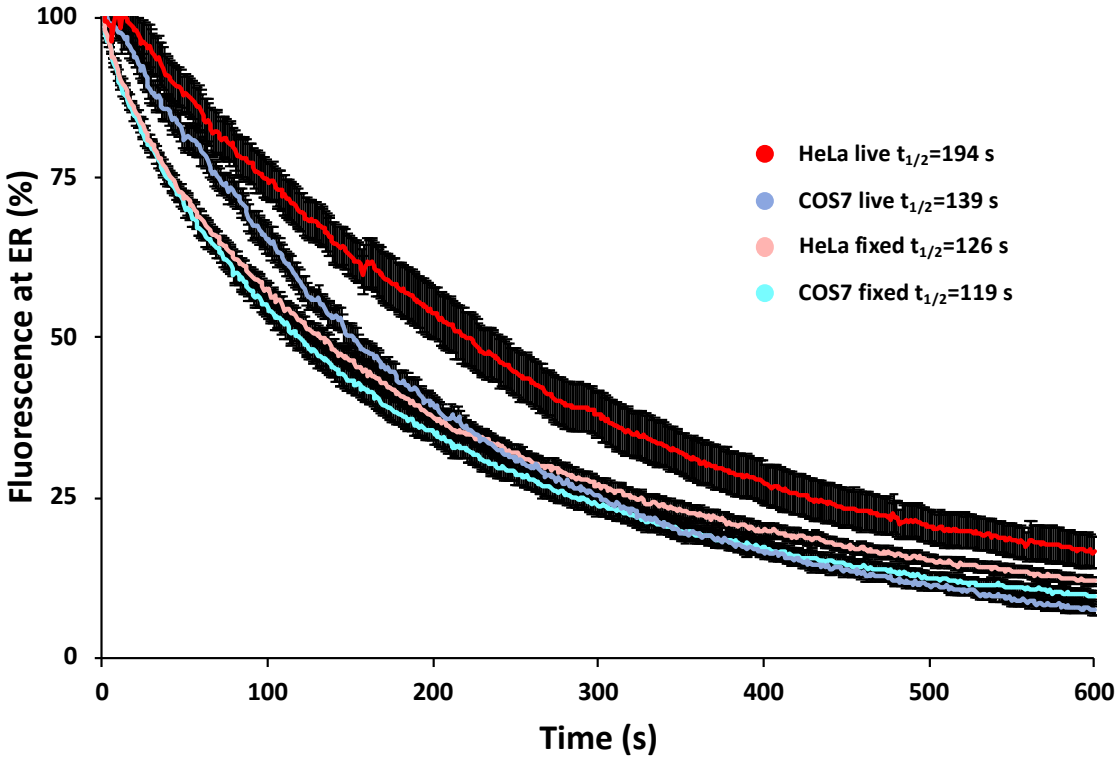

Supplementary Figure SN4.2
Bleaching of the transiently expressed SNAP-Sec61β in live and fixed COS7 and HeLa cells during STED-illumination. COS7 and HeLa cells transfected with 5 µg SNAP-Sec61β were labeled with 5 µM SiR-BG and imaged for 10 min. HeLa and COS7 cells were either imaged live in Live Cell Imaging Buffer or after a 15 min fixation in 3% paraformaldehyde and 0.1% glutaraldehyde in PBS. COS7 and HeLa live (N=9); COS7 and HeLa fixed

(N=8). The circles represent the mean values. Error bars represent standard errors of the mean (SEM). Standard errors: HeLa live $t_{1/2}$=194±4 s; COS7 live $t_{1/2}$=139±1 s; HeLa fixed $t_{1/2}$=126±1 s; COS7 fixed $t_{1/2}$=119±1 s. Independent experiments: HeLa live: 3, COS7 live: 2, Hela and COS7 fixed: 1

Supplementary Note 5: Fast resonant scanning reduces photodamage

One way to reduce photodamage by hardware-optimization is to reduce the time the laser focus dwells on any particular position in the sample and to give the exposed location time to recover before it is exposed again[153,154].

The T-Rex technique (triplet relaxation), for example, uses low repetition-rate lasers to reduce photobleaching in STED microscopy by preventing triplet-state build-up of fluorophores, which are highly reactive[128,155]. Random-access scanning, on the other hand, uses scan units that simultaneously image multiple points or line segments, which provides higher spatial resolution and further reduces photobleaching by reducing the total illumination time[156,157].

Alternatively, resonant scanning mirrors move the focus more quickly across the sample than conventional galvanometer scanners, which decreases the pixel dwell time and thereby prevents triplet-state build-up[1,153]. Using electro-optical deflectors allows even faster scanning[154]. The usage of the resonant scanner is advantageous because it is already implemented in many commercially available STED microscopes (see **Fig. 1c** and **Supplementary Fig. SN2c**)

To quantify the effect of faster scanning on cell stress, we imaged HeLa and COS7 cells transfected with SNAP-Sec61β and labeled with SiR-BG as described above with our custom-build STED microscope which features a 16-kHz resonance scanner[1] and compared the results to data recorded with a Leica TCS SP5 STED at 1-kHz scan speed. The imaging parameters on the custom-built STED microscope were chosen to be equivalent to the ones on the SP5, except for (i) an even higher value was chosen for the STED laser power on the custom instrument (140 mW instead of 40 mW) and (ii) a smaller scan field led to more light illuminating the imaged cell rather than areas around it. To obtain similar frame rates, we adjusted the line averaging when using the 16-kHz scanner (see **Supplementary Table SN5.1** below).

Supplementary Fig. SN5.1a,**b** show the FluoForte response of 19-20 cells imaged for each condition (9-10 HeLa and 10 COS7 cells each). The image acquisition at 1 kHz line scan speed caused a markedly higher Ca^{2+} response than the image acquisition at 16 kHz line scan speed. At 1 kHz, 80% of the COS7 cells showed problematic Ca^{2+}

response levels in the first 100 s of exposure (**Supplementary Fig. SN5.1a**, blue curves). For HeLa cells, 67% showed problematic Ca^{2+} response levels (**Supplementary Fig. SN5.1b**, red curves). Imaging COS7 and HeLa cells at 16 kHz caused considerably lower Ca^{2+} responses of both cell lines with 100% of the COS7 cells showing only a low or no response (**Supplementary Fig. SN5.1b**, blue curves). 90% of the HeLa cell showed a low or no response and only 1 out of 10 a problematic level of response (**Supplementary Fig. SN5.1b**, red curves). The addition of the ROS scavenging buffer described above further decreased the Ca^{2+} response of both cell lines leading to 100% of both cell lines showing only a low or no response (**Supplementary Fig. SN5.1c**).

We therefore recommend fast line scan speeds, if available, to minimize photodamage. The application of a ROS scavenging buffer can further be beneficial in minimizing photodamage.

Imaging Parameters	**Leica TCS SP5 STED**	**Custom-built STED**
Line scan speed	1 kHz	16 kHz
Line averages	1	32
Scan mode	unidirectional	unidirectional
Number of pixels	1024 x 1024	512 x 512
Frame rate	~1 Hz	0.989 Hz
Field of view	50.2 µm x 50.2 µm	25.6 µm x 25.6 µm
Excitation wavelength	635 nm (pulsed, 80 MHz)	650 nm (pulsed, 80 MHz)
Excitation laser power	20 µW	20 µW
Depletion wavelength	775 nm (pulsed, 80 MHz)	775 nm (pulsed, 80 MHz)
Depletion laser power	40 mW	140 mW

Supplementary Table SN5.1

Imaging parameters of the Leica TCS SP5 STED and our custom-built STED microscope.

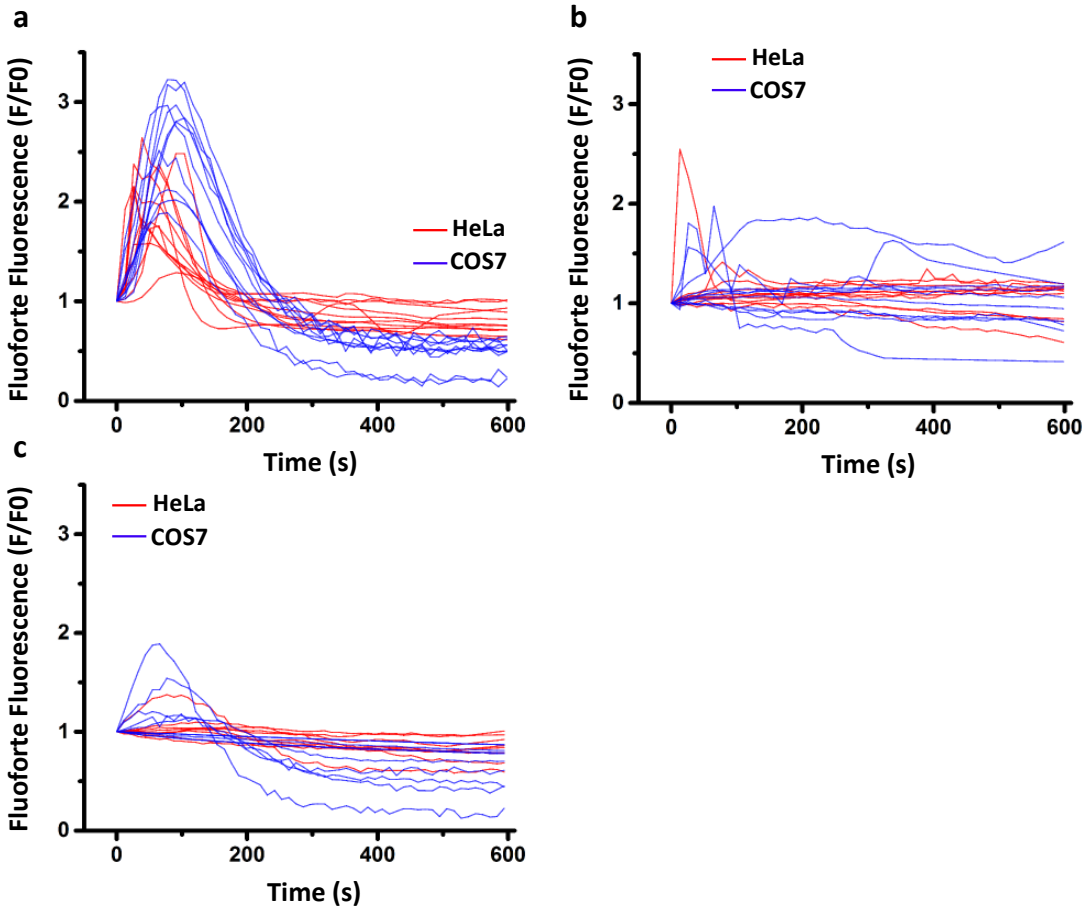

Supplementary Figure SN5.1

*HeLa (red) and COS7 (blue) cells transfected with 5 µg SNAP-Sec61β plasmid were labeled with 5 µM SiR-BG, incubated with FluoForte and monitored for 10 min. Cells were irradiated under standard (1 kHz line scan frequency) STED imaging conditions. 67% (6 out of N=9) and 80% (8 out of N=10) of the HeLa and COS7 cells, respectively, showed Ca^{2+}-level increases that we consider problematic (>2-fold FluoForte signal increase; see **Supplementary Note 2**) within the first 100 s **(a)**. In contrast, cells irradiated under STED imaging conditions with a faster scanner (16 kHz line scan frequency) responded less dramatically with 90% (9 out of N=10) of the HeLa cells and all (10 out of N=10) COS7 cells showing low or no measurable Ca^{2+} level increase **(b)**. With the addition of the ROS scavenging buffer the situation improved further with 100% of both cell lines showing low or no measurable Ca^{2+} level increase **(c)**. Three independent experiments were conducted for both cell lines in (a-c).*

Supplementary Note 6: Ca^{2+} release patterns depend on the location of SiR-labeling

Multiple factors can lead to cytoplasmic Ca^{2+} increase as a result of compartment damage during the imaging process. The amount and location of fluorescent probes in the cell play a particularly crucial role in this context[82]. To assess the damage potential of the SiR dye in relation to various compartments in our HeLa and COS7 cell systems, we imaged transiently transfected and labeled marker proteins of a range of compartments including the cytoplasm, Golgi apparatus, mitochondria and nucleus with SiR-BG (**Supplementary Fig. SN6.1**). Samples were imaged with a Leica TCS SP5 STED at 1 kHz line scan speed and without application of the ROS scavenging buffer described in **Supplementary Note 3**.

Imaging of the overexpressed soluble SNAP protein (pSNAP) in the cytoplasm and the SNAP-tagged OMP25 at the outer membrane of the mitochondria[158] revealed a rapid increase of cytoplasmic Ca^{2+} levels. Cytoplasmic Ca^{2+} levels began to rise within seconds after start of the imaging experiment indicating a very quick response of the cells to the light exposure (**Supplementary Fig. SN6.1a,b)**. This Ca^{2+} increase pattern is comparable to the observed patterns when imaging SiR-labeled SNAP-Sec61β (**Supplementary Fig. SN8.1a,b**) or when cells were treated with TG or IO (**Supplementary Fig. SN2.1c,d**). However, the increase of cytoplasmic Ca^{2+} levels was not as severe as it had been observed in these experiments, which can be explained by lower total amounts of expressed SNAP protein and consequently SiR in the cells (see below).

Interestingly, imaging SiR-labeled ManII-SNAP (α-mannosidase II, encoded by *Man2a1*), a marker of the *medial*- and *trans*-cisternae of the Golgi apparatus[159], caused a delayed release of a rather low amount of Ca^{2+} approximately 200 s after start of imaging (**Supplementary Fig. SN6.1c**).

The most delayed and most dramatic increase of cytoplasmic Ca^{2+} levels was observed when the SNAP-tagged histone H2B[160] was imaged (**Supplementary Fig. SN6.1d**). The imaging of the nucleus caused a delayed, but strong and sustained release of Ca^{2+}. The curves of the Ca^{2+} release that were obtained during the imaging of H2B-SNAP

resembled to some extend the curves that were obtained during the imaging of the AntA-treated cells (**Supplementary Fig. SN2.1b**).

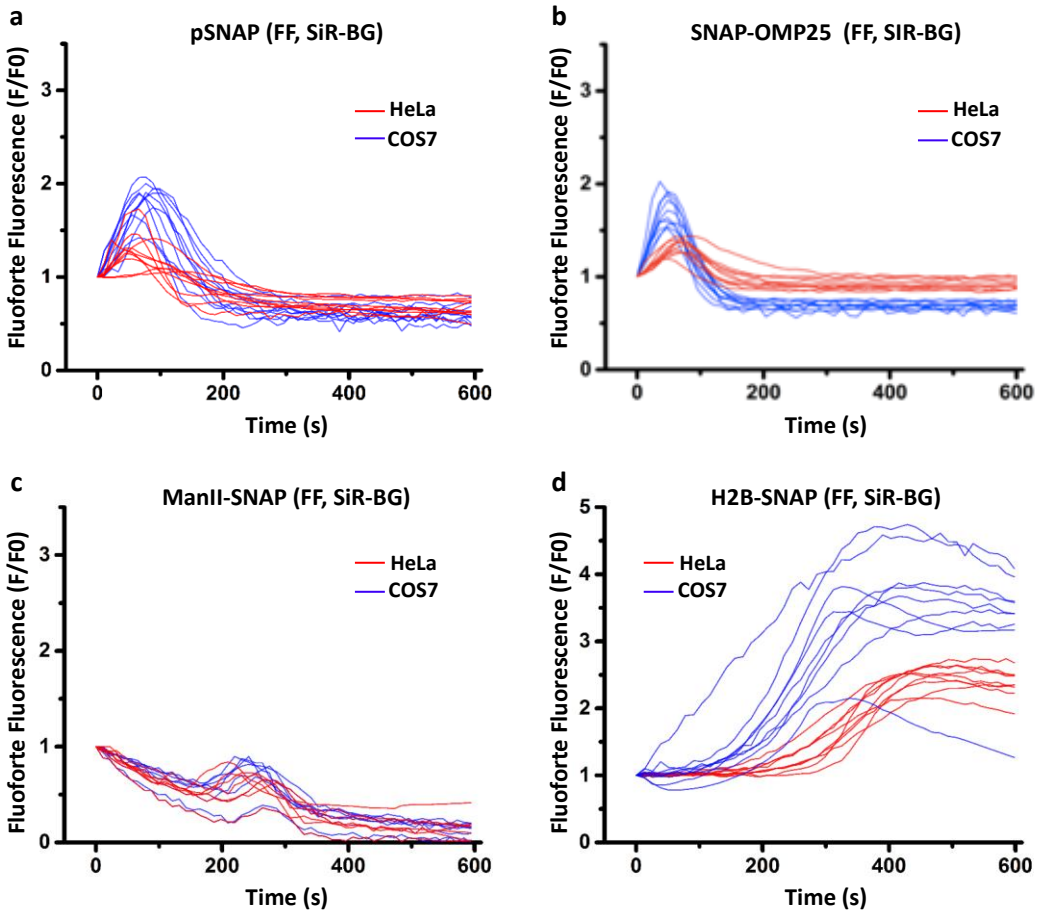

Supplementary Figure SN6.1

Ca^{2+} release patterns depend on the location of SiR-labeling. HeLa (red) and COS7 (blue) cells were transiently transfected with 5 µg of pSNAP (HeLa N=10, COS7 N=10). ***(a)****, SNAP-OMP2 (HeLa N=10, COS7 N=10)* ***(b)****, ManII-SNAP (HeLa N=7, COS7 N=7)* ***(c)*** *and H2B-SNAP plasmid (HeLa N=9, COS7 N=9)* ***(d)****, labeled with 5 µM SiR-BG, incubated with FluoForte and monitored for 10 min. Three independent experiments were conducted for both cell lines in (a-d).*

Supplementary Note 7: The Ca^{2+} level increase correlates with the level of labeling

Supplementary Fig. SN7.1 shows the level of the FluoForte response of HeLa and COS7 cells expressing different SNAP-tagged marker proteins of various cell organelles as a function of the total amount of dye in each cell. The Figure reveals a striking correlation between the total amount of dye and the imaging-induced damage of the cell. This trend is visible within each group of cells expressing varying levels of the same construct, but also is reflected by the fact that, for example, cells expressing SNAP-OMP25 generally show both a lower level of SiR-labeling as well as lower FluoForte responses than cells transiently expressing SNAP-Sec61β. Strikingly, for most labels we do not see considerable differences between COS7 and HeLa cells. With the exception of the histone H2B-SNAP labeled COS7 cells, all cells follow the same linear trend.

Our results suggest that the observed cell damage is mediated directly through light-absorption by the dye during image acquisition. It is important to note in this context that the used wavelengths are all in the red spectrum (>630 nm). At lower wavelengths, in general, a large number of cellular components absorbs light and therefore contribute to cellular damage, probably leading to a less pronounced correlation (see also **Supplementary Note 8**).

The general function of the imaged compartment in Ca^{2+} homeostasis, as well as the localization of the SNAP-tagged protein in relation to the compartment membrane, might be potential additional factors in the overall picture of cell damage and need to be further investigated.

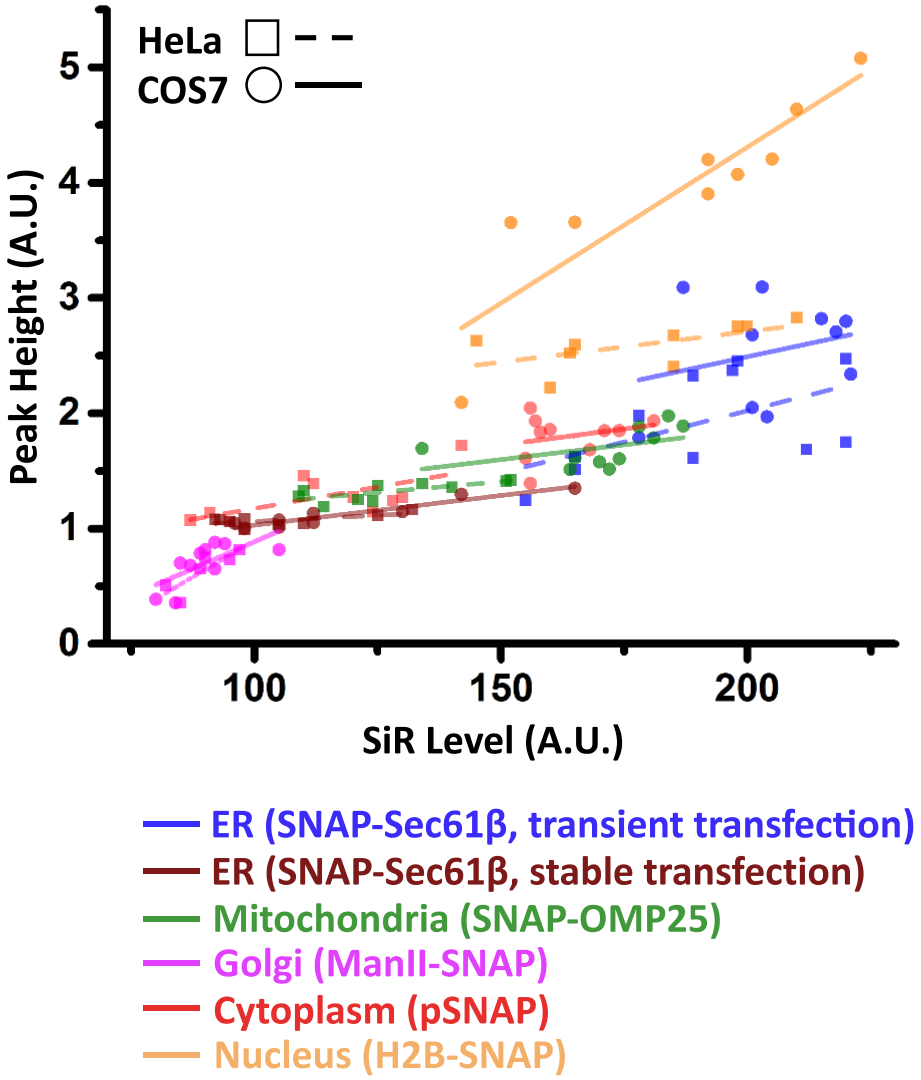

Supplementary Figure SN7.1

The level of Ca^{2+} increase is strongly correlated to the labeling level and (to a lesser extend) the location of the dye. HeLa and COS7 cells were stably or transiently transfected with 5 µg SNAP-Sec61β, pSNAP, SNAP-OMP25, ManII-SNAP and H2B-SNAP plasmid, labeled with 5 µM SiR-BG, incubated with FluoForte and monitored for about 10 min. The data represented in ***Supplementary Fig. SN6.1, SN8.1a,b*** *were used to generate this figure. Please refer to these figure captions for numbers of cells.*

Supplementary Note 8: Transient vs. stable transfections

Transient transfection is the method of choice when it comes to a temporary, usually CMV promoter-driven (human *Cytomegalovirus* immediate-early enhancer and promoter), overexpression of genes in mammalian cells. The most commonly used methods for transient transfection are liposome-based DNA-carriers such as Lipofectamine or electroporation. However, transient transfection is another widely appreciated cell-harming factor that can cause a preceding damage of the cells before the actual imaging experiment is conducted due to the induction of cell stress responses and changes in gene expression pattern[82,161].

To investigate the potential damaging effect of transient transfections, we compared FluoForte levels in stably and transiently transfected cells. We generated stable HeLa and COS7 cell lines that overexpress the SNAP-tagged SEC61B gene under a CMV promoter (see **Supplementary Methods**) and labeled and imaged them in the same way as in the experiments described above (see **Supplementary Note 6** and **7**) using transient transfection.

As shown in **Supplementary Fig. SN7.1**, the stably expressing cells show on average lower expression levels and lower damage responses than their transiently expressing counter-parts. The data points fall within the linear distribution shown in this figure which, as discussed in **Supplementary Note 7**, suggests that the lower damage response in the stably expressing cells can be explained by the reduced SiR level and that the stress contribution from electroporation and transient transfection is only minor.

Additional experiments comparing transiently transfected, unlabeled cells with non-transfected cells (**Supplementary Fig. SN8.1c,d**) reveal a negligible to weak damage response caused by the transfection, confirming this observation.

We nonetheless suggest the generation of stable cell lines (**Supplementary Methods**) where possible since the lower levels of staining lead to less photodamage. Even better is the application of the CRISPR/Cas9 system (Clustered regularly interspaced short palindromic repeats/CRISPR-associated protein-9 nuclease) to express the tagged protein of interest at endogenous levels[162].

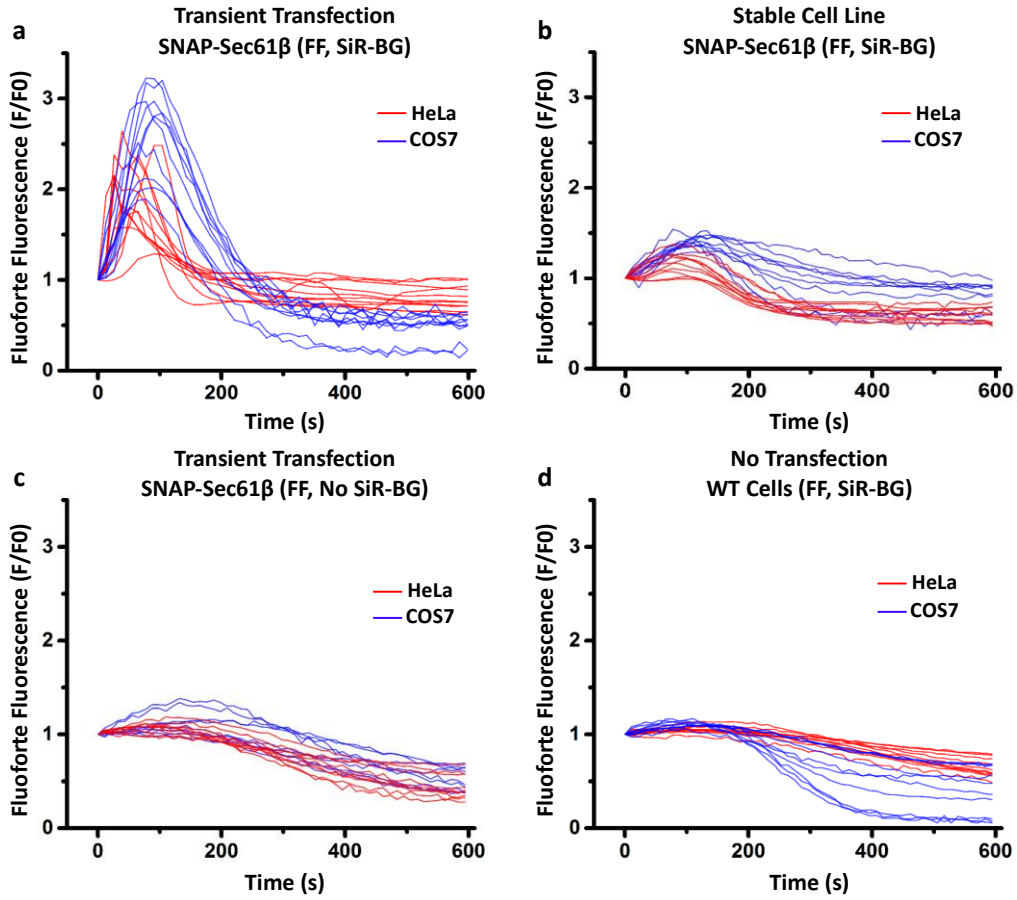

Supplementary Figure SN8.1

FluoForte response curves for HeLa (red) and COS7 (blue) cells transiently transfected with 5 µg of SNAP- Sec61β plasmid, labeled with 5 µM SiR-BG and incubated with FluoForte (HeLa N=9, COS7 N=10) ***(a)****, cells stably transfected with SNAP-Sec61β and labeled with 5µM SiR-BG (HeLa N=10, COS7 N=10)* ***(b)****, cells transfected as described in (a) but not labeled with 5 µM SiR-BG (HeLa N=9, COS7 N=9)* ***(c)****, and non-transfected cells (HeLa N=10, COS7 N=10)* ***(d)****. Three independent experiments were conducted for both cell lines in (a-d).*

Supplementary Note 9: Imaging with a shorter wavelength at 458 nm leads to high damage response levels

It is widely appreciated that short irradiation wavelengths generally cause greater photodamage to cells than long wavelengths[82,84]. Photons with shorter wavelengths possess a higher energy, which increases the chance of initiating chemical breakdown of fluorophores[84]. Another mechanism involves the long-living triplet-state or dark state of the fluorophores that show different absorption spectra and tend to absorb shorter wavelengths with higher efficiency leading to high-energy states, which are more prone to bleach[84,163]. Furthermore, many endogenous molecules, including many proteins and DNA, can absorb high-energy photons and thereby cause labeling-independent photo-damage.

We imaged samples prepared in the same way as for the described STED experiments (e.g. **Supplementary Fig. SN6.1 and Supplementary Fig. SN8.1 a,b**) and imaged them on our Leica TCS SP5 STED microscope with 458-nm excitation wavelength at approximately 11 µW laser power. All cells were labeled with 5 µM SiR-BG and incubated with the red-shifted FluoForte (GFP-certified FluoForte). The corresponding damage response curves are shown in **Supplementary Fig. SN9.1**. We consistently observed problematic Ca^{2+} response levels. Compared to the results obtained in the STED experiments presented in **Supplementary Note 6** and **Supplementary Note 8**, the shape of the Ca^{2+} response curves is more uniform and less dependent on the labeled target proteins. This suggests that the observed 458-nm light-induced damage is primarily not relayed through the SiR dye but through natural cellular components.

These results emphasize the importance of the wavelength when designing live-cell experiments. We suggest avoiding the excessive use of short wavelengths.

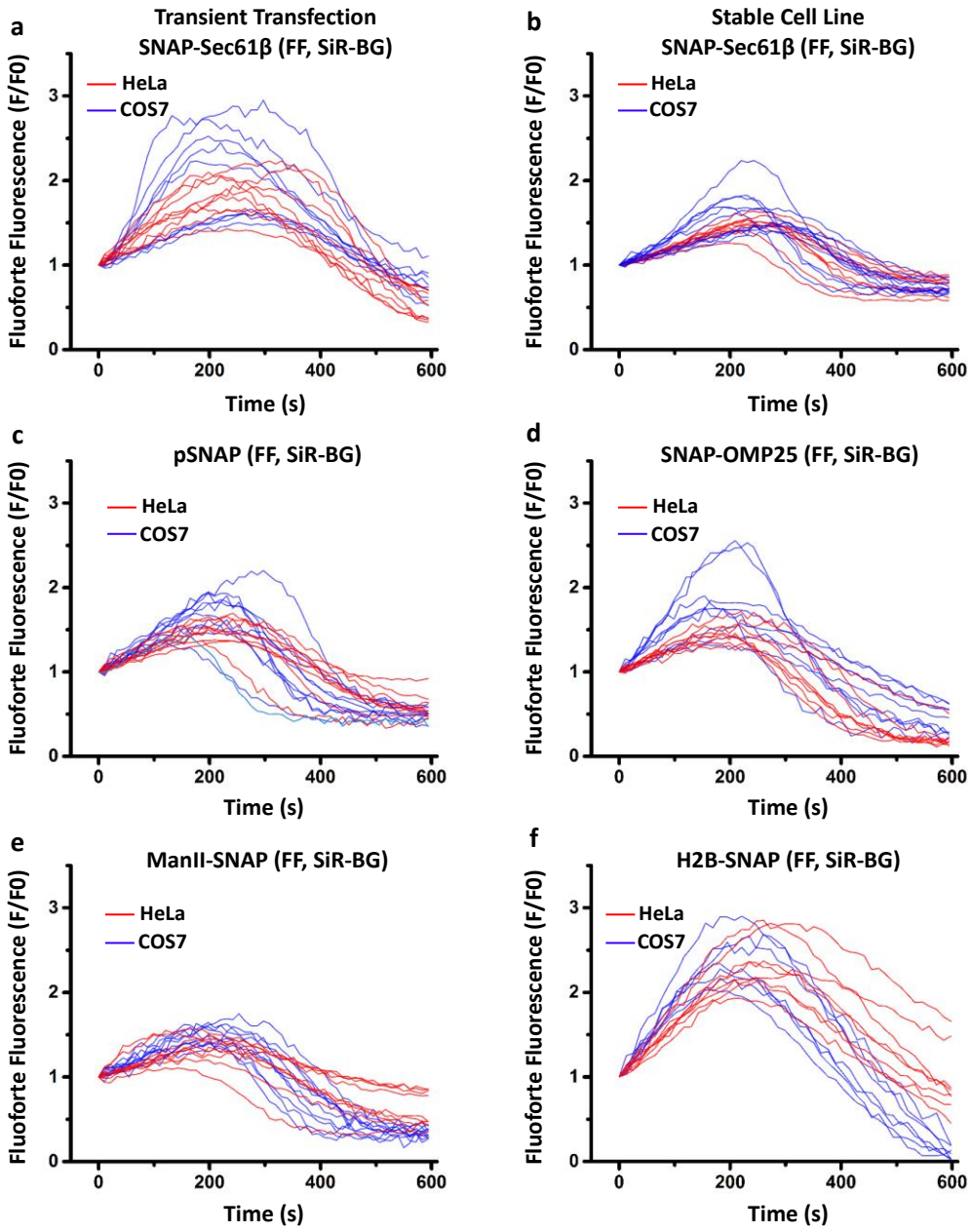

Supplementary Figure SN9.1

Damage response curves of cells imaged with a 458-nm laser (but no STED light). HeLa (red) and COS7 (blue) cells transiently or stably transfected with SNAP-Sec61β ***(a,b)****. Transiently overexpressed pSNAP, SNAP-OMP25, ManII-SNAP and H2B-SNAP* ***(c-f)****. All cells were labeled with 5 μM SiR-BG and incubated with the red-shifted FluoForte (GFP-certified FluoForte). The more uniform shape of the curves compared to* ***Supplementary Fig. SN6.1*** *and* ***Supplementary Fig. SN8.1a,b*** *suggests a more general damage pathway not mediated by the SiR dye. (HeLa N=9, COS7 N=9) (a),(HeLa N=10, COS7 N=10) (b), (HeLa N=8, COS7 N=11) (c), (HeLa N=8, COS7 N=9) (d), (HeLa N=9, COS7 N=10) (e), (HeLa N=8, COS7 N=7) (f). Three independent experiments were conducted for both cell lines in (a-f).*

Supplementary Note 10: Resolution of STED videos

STED microscopy of SNAP-tagged and SiR-labeled proteins allows the examination of living cells with a resolution below 50 nm[1].

To determine the resolution of the Leica TCS SP8 STED 3X, we analyzed the first frame of a representative COS7 cell video (**Supplementary Video 1**) with a newly developed technique (Nested-loop Ensemble PSF (NEP) fitting) that allowed us to measure the resolution based on the ER membrane labeling in live cells[5] (**Supplementary Fig. SN10.1a**). The full-width-at-half-maximum of the point-spread function determined by NEP fitting is 44 nm (**Supplementary Fig. SN10.1b**).

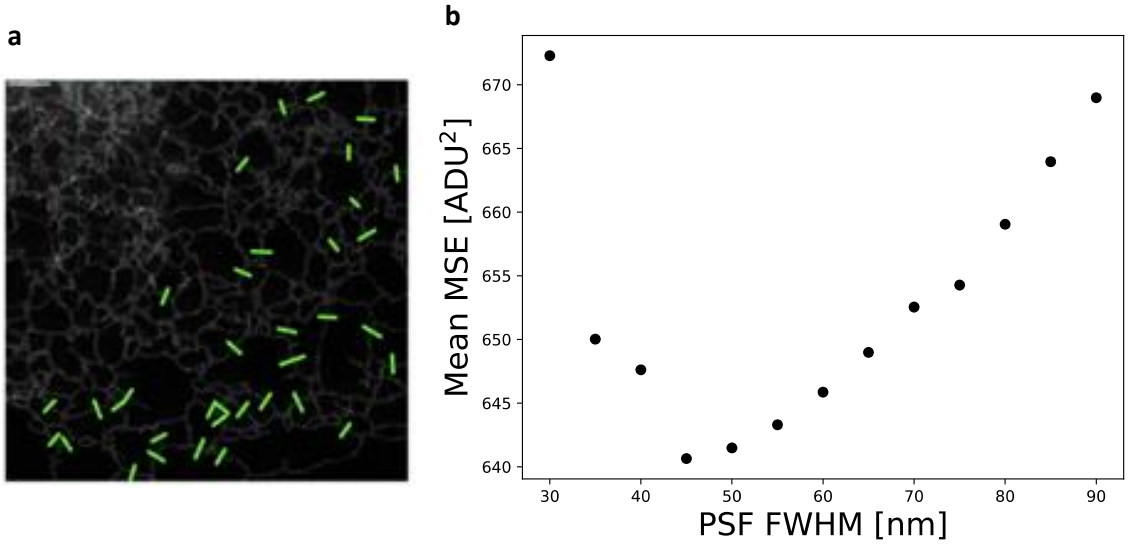

Supplementary Figure SN10.1
Estimation of resolution for acquired STED videos.
(a) *First frame of Supplementary Video 1 showing SiR-labeled Sec61β in a live COS7 cell imaged with STED at the same laser intensities as used in Fig. 1 (scale bar: 3 µm). Representative video out of N=5, 1 independent experiment.* ***(b)*** *The full-width at half-maximum of the STED point-spread function is estimated to be 44 nm based on the location of the minimum in the mean MSE curve. 36 line profiles taken from the first video frame were used for the analysis. The quantitative analysis was not repeated in this study but is consistent with Barentine et al.*[5].

Supplementary Note 11: Long-term viability of STED-irradiated COS7 and HeLa cells

Only very few of the examined cells in our various FluoForte Ca^{2+} response experiments showed a strong Ca^{2+} response during the about 10 min of STED irradiation (**Fig. 1c**, **Supplementary Fig. SN2.2 c**, **Supplementary Fig. SN5.1b**). To determine, if the initial STED irradiation had any effects on the long-term viability of the examined cells, we examined the viability of STED-irradiated HeLa and COS7 cells for 24 h after the original imaging experiment by using a LCV110 VivaView Incubator Microscope (Olympus). Our results are summarized in **Fig. 1m**. The experiments are described in the **Supplementary Methods**.

These experiments also enabled us to investigate the predictive value of Ca^{2+}-measurements for a cell's long-term survival. Our data shows, first, that cells that exhibited no significant Ca^{2+}-increase during STED irradiation could still die within the next 24-30 h (black curves which stayed below F/F0=2 in **Supplementary Fig. SN11.1**). This is not surprising given that we saw the same phenomenon for our negative control cells (**Fig. 1m**) and the fact that the trigger for cell death could occur at any time before death, not just during the 10-min window when we monitored FluoForte. Second, all surviving cells (green curves in **Supplementary Fig. SN11.1**) had exhibited Ca^{2+}-levels staying below the critical F/F0=2 threshold. Third, cells that had exhibited problematic Ca^{2+}-levels either died in the following 24-30 h or their fate was indeterminable (magenta curves in **Supplementary Fig. SN11.1**). We did not observe a cell surviving after it had shown a problematic Ca^{2+}-response. High Ca^{2+}-response values are therefore suggestive of cell death in the next 24-30 h, in particular if we assume that most indeterminable cell fates represented cell deaths.

Overall, while about 25% of STED-irradiated cells survive beyond 24 h, a substantial number dies. Not all of these cell deaths can be attributed to STED irradiation, as our control experiments in **Fig. 1m** show, but some can. A straight-forward strategy to reduce this number is the reduction of STED exposure. Instead of continuous irradiation for 10 min, one can image for shorter durations or take time-lapse sequences with intervals

of no laser exposure, for example STED images recorded once per minute for 10 minutes, resulting in 10 instead of about 600 images.

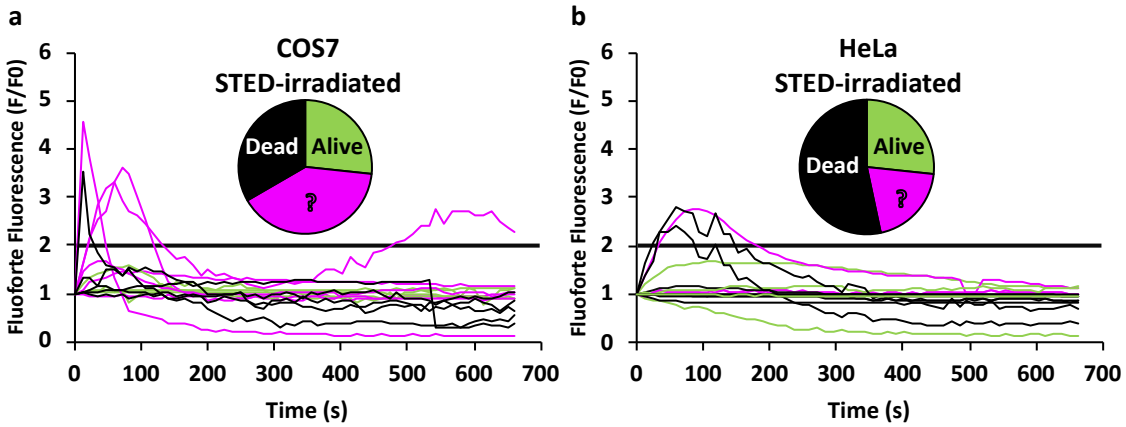

Supplementary Figure SN11.1
Correlation of individual Ca^{2+} response during STED irradiation and later fate of HeLa and COS7 cells after 24 h. COS7 N=15 (a), HeLa N=15 (b). Three independent experiments were conducted for both cell lines.

SUPPLEMENTARY REFERENCES:

1 Bottanelli, F. *et al.* Two-colour live-cell nanoscale imaging of intracellular targets. *Nat Commun* **7**, 10778, doi:10.1038/ncomms10778 (2016).

2 Jacobson, J. & Duchen, M. R. Mitochondrial oxidative stress and cell death in astrocytes--requirement for stored Ca2+ and sustained opening of the permeability transition pore. *J Cell Sci* **115**, 1175-1188 (2002).

3 Swoboda, M. *et al.* Enzymatic oxygen scavenging for photostability without pH drop in single-molecule experiments. *ACS Nano* **6**, 6364-6369, doi:10.1021/nn301895c (2012).

4 Crivat, G. & Taraska, J. W. Imaging proteins inside cells with fluorescent tags. *Trends in Biotechnology* **30**, 8-16, doi:http://dx.doi.org/10.1016/j.tibtech.2011.08.002 (2012).

5 Barentine, A. S., Schroeder, L., Graff, M., Baddeley, D. & Bewersdorf, J. Simultaneously measuring image features and resolution in live-cell STED images. *Biophysical Journal*, doi:10.1016/j.bpj.2018.07.028 (2018).

6 Verkhratsky, A. Physiology and Pathophysiology of the Calcium Store in the Endoplasmic Reticulum of Neurons. *Physiological Reviews* **85**, 201-279, doi:10.1152/physrev.00004.2004 (2005).

7 Pinton, P., Giorgi, C., Siviero, R., Zecchini, E. & Rizzuto, R. Calcium and apoptosis: ER-mitochondria Ca2+ transfer in the control of apoptosis. *Oncogene* **27**, 6407-6418, doi:10.1038/onc.2008.308 (2008).

8 Rizzuto, R. & Pozzan, T. Microdomains of intracellular Ca2+: molecular determinants and functional consequences. *Physiol Rev* **86**, 369-408, doi:10.1152/physrev.00004.2005 (2006).

9 Berridge, M. J., Bootman, M. D. & Lipp, P. Calcium--a life and death signal. *Nature* **395**, 645-648, doi:10.1038/27094 (1998).

10 Nowycky, M. C. & Thomas, A. P. Intracellular calcium signaling. *J Cell Sci* **115**, 3715-3716 (2002).

11 Barbado, M., Fablet, K., Ronjat, M. & De Waard, M. Gene regulation by voltage-dependent calcium channels. *Biochim Biophys Acta* **1793**, 1096-1104, doi:10.1016/j.bbamcr.2009.02.004 (2009).

12 Zivadinovic, D., Tomic, M., Yuan, D. & Stojilkovic, S. S. Cell-Type Specific Messenger Functions of Extracellular Calcium in the Anterior Pituitary. *Endocrinology* **143**, 445-455, doi:10.1210/endo.143.2.8637 (2002).

13 He, H., Kong, S. K. & Chan, K. T. Identification of source of calcium in HeLa cells by femtosecond laser excitation. *J Biomed Opt* **15**, 057010, doi:10.1117/1.3485741 (2010).

14 Dupont, G., Combettes, L., Bird, G. S. & Putney, J. W. Calcium oscillations. *Cold Spring Harbor perspectives in biology* **3**, doi:10.1101/cshperspect.a004226 (2011).

15 Iwanaga, S. *et al.* Location-dependent photogeneration of calcium waves in HeLa cells. *Cell Biochem Biophys* **45**, 167-176, doi:10.1385/CBB:45:2:167 (2006).

16 Berridge, M. J., Lipp, P. & Bootman, M. D. The versatility and universality of calcium signalling. *Nat Rev Mol Cell Biol* **1**, 11-21 (2000).

17 Samtleben, S. *et al.* Direct Imaging of ER Calcium with Targeted-Esterase Induced Dye Loading (TED). e50317, doi:doi:10.3791/50317 (2013).
18 Nicotera, P. & Verkhratsky, A. Calcium Signals in Cell Death and Disease. *J Physiol Sci* **59**, 93-93 (2009).
19 Bootman, M. D. Calcium signaling. *Cold Spring Harbor perspectives in biology* **4**, a011171, doi:10.1101/cshperspect.a011171 (2012).
20 Clapham, D. E. Calcium signaling. *Cell* **131**, 1047-1058, doi:10.1016/j.cell.2007.11.028 (2007).
21 Diliberto, P. A., Wang, X. F. & Herman, B. in *Methods in cell biology* Vol. Volume 40 (ed Nuccitelli Richard) 243-262 (Academic Press, 1994).
22 Zong, W. X. & Thompson, C. B. Necrotic death as a cell fate. *Genes & development* **20**, 1-15, doi:10.1101/gad.1376506 (2006).
23 Brookes, P. S., Yoon, Y., Robotham, J. L., Anders, M. W. & Sheu, S. S. Calcium, ATP, and ROS: a mitochondrial love-hate triangle. *Am J Physiol Cell Physiol* **287**, C817-833, doi:10.1152/ajpcell.00139.2004 (2004).
24 Chaudhari, N., Talwar, P., Parimisetty, A., d'Hellencourt, C. L. & Ravanan, P. A molecular web: endoplasmic reticulum stress, inflammation, and oxidative stress. *Front Cell Neurosci* **8**, 213, doi: 10.3389/fncel.2014.00213 (2014).
25 Contreras, L., Drago, I., Zampese, E. & Pozzan, T. Mitochondria: The calcium connection. *Biochimica et Biophysica Acta (BBA) - Bioenergetics* **1797**, 607-618, doi:http://dx.doi.org/10.1016/j.bbabio.2010.05.005 (2010).
26 Aulestia, Francisco J., Alonso, María T. & García-Sancho, J. Differential calcium handling by the cis and trans regions of the Golgi apparatus. *Biochemical Journal* **466**, 455-465, doi:10.1042/bj20141358 (2015).
27 Van Baelen, K. *et al.* The Ca2+/Mn2+ pumps in the Golgi apparatus. *Biochimica et Biophysica Acta (BBA) - Molecular Cell Research* **1742**, 103-112, doi:http://dx.doi.org/10.1016/j.bbamcr.2004.08.018 (2004).
28 Rizzuto, R., De Stefani, D., Raffaello, A. & Mammucari, C. Mitochondria as sensors and regulators of calcium signalling. *Nat Rev Mol Cell Biol* **13**, 566-578, doi:10.1038/nrm3412 (2012).
29 Koch, G. L. The endoplasmic reticulum and calcium storage. *BioEssays : news and reviews in molecular, cellular and developmental biology* **12**, 527-531, doi:10.1002/bies.950121105 (1990).
30 Melino, G. The Sirens' song. *Nature* **412**, 23, doi:10.1038/35083653 (2001).
31 Kroemer, G. *et al.* Classification of cell death: recommendations of the Nomenclature Committee on Cell Death 2009. *Cell Death Differ* **16**, 3-11, doi:10.1038/cdd.2008.150 (2009).
32 Zhivotovsky, B. & Orrenius, S. Clinical perspectives of cell death: where we are and where to go. *Apoptosis : an international journal on programmed cell death* **14**, 333-335, doi:10.1007/s10495-009-0326-x (2009).
33 Galluzzi, L. *et al.* Molecular definitions of cell death subroutines: recommendations of the Nomenclature Committee on Cell Death 2012. *Cell Death Differ* **19**, 107-120, doi:10.1038/cdd.2011.96 (2012).
34 Festjens, N., Vanden Berghe, T. & Vandenabeele, P. Necrosis, a well-orchestrated form of cell demise: signalling cascades, important mediators

and concomitant immune response. *Biochim Biophys Acta* **1757**, 1371-1387, doi:10.1016/j.bbabio.2006.06.014 (2006).
35 Harr, M. W. & Distelhorst, C. W. Apoptosis and autophagy: decoding calcium signals that mediate life or death. *Cold Spring Harbor perspectives in biology* **2**, a005579, doi:10.1101/cshperspect.a005579 (2010).
36 Orrenius, S., Zhivotovsky, B. & Nicotera, P. Regulation of cell death: the calcium-apoptosis link. *Nat Rev Mol Cell Biol* **4**, 552-565, doi:10.1038/nrm1150 (2003).
37 Fleckenstein, A., Janke, J., Doring, H. J. & Leder, O. Myocardial fiber necrosis due to intracellular Ca overload-a new principle in cardiac pathophysiology. *Recent advances in studies on cardiac structure and metabolism* **4**, 563-580 (1974).
38 Galluzzi, L. *et al.* Cell death modalities: classification and pathophysiological implications. *Cell Death Differ* **14**, 1237-1243, doi:10.1038/sj.cdd.4402148 (2007).
39 Zhivotovsky, B. & Orrenius, S. Calcium and cell death mechanisms: a perspective from the cell death community. *Cell Calcium* **50**, 211-221, doi:10.1016/j.ceca.2011.03.003 (2011).
40 Sun, F., Xu, X., Wang, X. & Zhang, B. Regulation of autophagy by Ca2. *Tumour biology : the journal of the International Society for Oncodevelopmental Biology and Medicine*, doi:10.1007/s13277-016-5353-y (2016).
41 Medina, D. L. *et al.* Lysosomal calcium signalling regulates autophagy through calcineurin and TFEB. *Nat Cell Biol* **17**, 288-299, doi:10.1038/ncb3114 (2015).
42 Kondratskyi, A. *et al.* Calcium-permeable ion channels in control of autophagy and cancer. *Frontiers in physiology* **4**, 272, doi:10.3389/fphys.2013.00272 (2013).
43 Broker, L. E., Kruyt, F. A. & Giaccone, G. Cell death independent of caspases: a review. *Clinical cancer research : an official journal of the American Association for Cancer Research* **11**, 3155-3162, doi:10.1158/1078-0432.CCR-04-2223 (2005).
44 Nicotera, P. & Orrenius, S. The role of calcium in apoptosis. *Cell Calcium* **23**, 173-180 (1998).
45 Schwarz, D. S. & Blower, M. D. The endoplasmic reticulum: structure, function and response to cellular signaling. *Cellular and molecular life sciences : CMLS* **73**, 79-94, doi:10.1007/s00018-015-2052-6 (2016).
46 Henderson, M. J., Wires, E. S., Trychta, K. A., Richie, C. T. & Harvey, B. K. SERCaMP: a carboxy-terminal protein modification that enables monitoring of ER calcium homeostasis. *Molecular biology of the cell* **25**, 2828-2839, doi:10.1091/mbc.E14-06-1141 (2014).
47 Mekahli, D., Bultynck, G., Parys, J. B., De Smedt, H. & Missiaen, L. Endoplasmic-reticulum calcium depletion and disease. *Cold Spring Harbor perspectives in biology* **3**, doi:10.1101/cshperspect.a004317 (2011).
48 Mattson, M. P. & Chan, S. L. Calcium orchestrates apoptosis. *Nat Cell Biol* **5**, 1041-1043, doi:10.1038/ncb1203-1041 (2003).

49 Kruman, I., Guo, Q. & Mattson, M. P. Calcium and reactive oxygen species mediate staurosporine-induced mitochondrial dysfunction and apoptosis in PC12 cells. *J Neurosci Res* **51**, 293-308 (1998).
50 Tombal, B., Denmeade, S. R. & Isaacs, J. T. Assessment and validation of a microinjection method for kinetic analysis of [Ca2+]i in individual cells undergoing apoptosis. *Cell Calcium* **25**, 19-28, doi:10.1054/ceca.1998.0005 (1999).
51 Scorrano, L. *et al.* BAX and BAK regulation of endoplasmic reticulum Ca2+: a control point for apoptosis. *Science* **300**, 135-139, doi:10.1126/science.1081208 (2003).
52 Koester, H. J., Baur, D., Uhl, R. & Hell, S. W. Ca2+ fluorescence imaging with pico- and femtosecond two-photon excitation: signal and photodamage. *Biophys J* **77**, 2226-2236, doi:10.1016/S0006-3495(99)77063-3 (1999).
53 Vance, J. E. MAM (mitochondria-associated membranes) in mammalian cells: lipids and beyond. *Biochim Biophys Acta* **1841**, 595-609, doi:10.1016/j.bbalip.2013.11.014 (2014).
54 Griffiths, E. J. & Rutter, G. A. Mitochondrial calcium as a key regulator of mitochondrial ATP production in mammalian cells. *Biochim Biophys Acta* **1787**, 1324-1333, doi:10.1016/j.bbabio.2009.01.019 (2009).
55 Pan, X. *et al.* The physiological role of mitochondrial calcium revealed by mice lacking the mitochondrial calcium uniporter. *Nat Cell Biol* **15**, 1464-1472, doi:10.1038/ncb2868 (2013).
56 Quan, X. *et al.* Essential role of mitochondrial Ca2+ uniporter in the generation of mitochondrial pH gradient and metabolism-secretion coupling in insulin-releasing cells. *J Biol Chem* **290**, 4086-4096, doi:10.1074/jbc.M114.632547 (2015).
57 Arnaudeau, S., Kelley, W. L., Walsh, J. V., Jr. & Demaurex, N. Mitochondria recycle Ca(2+) to the endoplasmic reticulum and prevent the depletion of neighboring endoplasmic reticulum regions. *J Biol Chem* **276**, 29430-29439, doi:10.1074/jbc.M103274200 (2001).
58 Malli, R., Frieden, M., Trenker, M. & Graier, W. F. The role of mitochondria for Ca2+ refilling of the endoplasmic reticulum. *J Biol Chem* **280**, 12114-12122, doi:10.1074/jbc.M409353200 (2005).
59 Yin, X.-M. & Dong, Z. *Essentials of apoptosis : a guide for basic and clinical research*. (Humana Press, 2003).
60 Cerella, C., Diederich, M. & Ghibelli, L. The dual role of calcium as messenger and stressor in cell damage, death, and survival. *International journal of cell biology* **2010**, 546163, doi:10.1155/2010/546163 (2010).
61 Morin, D., Pires, F., Plin, C. & Tillement, J. P. Role of the permeability transition pore in cytochrome C release from mitochondria during ischemia-reperfusion in rat liver. *Biochemical pharmacology* **68**, 2065-2073, doi:10.1016/j.bcp.2004.07.006 (2004).
62 Nikoletopoulou, V., Markaki, M., Palikaras, K. & Tavernarakis, N. Crosstalk between apoptosis, necrosis and autophagy. *Biochim Biophys Acta* **1833**, 3448-3459, doi:10.1016/j.bbamcr.2013.06.001 (2013).

63 Choi, D. W. Calcium: still center-stage in hypoxic-ischemic neuronal death. *Trends in neurosciences* **18**, 58-60 (1995).
64 Osellame, L. D., Blacker, T. S. & Duchen, M. R. Cellular and molecular mechanisms of mitochondrial function. *Best practice & research. Clinical endocrinology & metabolism* **26**, 711-723, doi:10.1016/j.beem.2012.05.003 (2012).
65 Ziegler, U. & Groscurth, P. Morphological features of cell death. *News in physiological sciences : an international journal of physiology produced jointly by the International Union of Physiological Sciences and the American Physiological Society* **19**, 124-128 (2004).
66 Pasparakis, M. & Vandenabeele, P. Necroptosis and its role in inflammation. *Nature* **517**, 311-320, doi:10.1038/nature14191 (2015).
67 Knot, H. J. *et al.* Twenty years of calcium imaging: cell physiology to dye for. *Molecular interventions* **5**, 112-127, doi:10.1124/mi.5.2.8 (2005).
68 Specht, K. G. & Rodgers, M. A. Plasma membrane depolarization and calcium influx during cell injury by photodynamic action. *Biochim Biophys Acta* **1070**, 60-68 (1991).
69 Yonuschot, G. Early increase in intracellular calcium during photodynamic permeabilization. *Free radical biology & medicine* **11**, 307-317 (1991).
70 Penning, L. C. *et al.* A role for the transient increase of cytoplasmic free calcium in cell rescue after photodynamic treatment. *Biochim Biophys Acta* **1107**, 255-260 (1992).
71 Ben-Her, E. & Dubbelman, T. M. Cytoplasmic free calcium changes as a trigger mechanism in the response of cells to photosensitization. *Photochem Photobiol* **58**, 890-894 (1993).
72 Ruck, A. *et al.* Light-induced apoptosis involves a defined sequence of cytoplasmic and nuclear calcium release in AlPcS4-photosensitized rat bladder RR 1022 epithelial cells. *Photochem Photobiol* **72**, 210-216, doi:10.1562/0031-8655(2000)072<0210:LIAIAD>2.0.CO;2 (2000).
73 Granville, D. J. *et al.* Bcl-2 increases emptying of endoplasmic reticulum Ca2+ stores during photodynamic therapy-induced apoptosis. *Cell Calcium* **30**, 343-350, doi:10.1054/ceca.2001.0243 (2001).
74 Tarr, M., Frolov, A. & Valenzeno, D. P. Photosensitization-induced calcium overload in cardiac cells: direct link to membrane permeabilization and calcium influx. *Photochem Photobiol* **73**, 418-424 (2001).
75 Robertson, C. A., Evans, D. H. & Abrahamse, H. Photodynamic therapy (PDT): a short review on cellular mechanisms and cancer research applications for PDT. *Journal of photochemistry and photobiology. B, Biology* **96**, 1-8, doi:10.1016/j.jphotobiol.2009.04.001 (2009).
76 Holmstrom, K. M. & Finkel, T. Cellular mechanisms and physiological consequences of redox-dependent signalling. *Nat Rev Mol Cell Biol* **15**, 411-421, doi:10.1038/nrm3801 (2014).
77 Gorlach, A. *et al.* Reactive oxygen species, nutrition, hypoxia and diseases: Problems solved? *Redox biology* **6**, 372-385, doi:10.1016/j.redox.2015.08.016 (2015).

78 Sokolovski, S. G. *et al.* Infrared laser pulse triggers increased singlet oxygen production in tumour cells. *Sci Rep* **3**, 3484, doi:10.1038/srep03484 (2013).
79 Zhou, X. *et al.* Laser controlled singlet oxygen generation in mitochondria to promote mitochondrial DNA replication in vitro. *Sci Rep* **5**, 16925, doi:10.1038/srep16925 (2015).
80 D'Autreaux, B. & Toledano, M. B. ROS as signalling molecules: mechanisms that generate specificity in ROS homeostasis. *Nat Rev Mol Cell Biol* **8**, 813-824, doi:10.1038/nrm2256 (2007).
81 Rodriguez, R. & Redman, R. Balancing the generation and elimination of reactive oxygen species. *Proc Natl Acad Sci U S A* **102**, 3175-3176, doi:10.1073/pnas.0500367102 (2005).
82 Waldchen, S., Lehmann, J., Klein, T., van de Linde, S. & Sauer, M. Light-induced cell damage in live-cell super-resolution microscopy. *Sci Rep* **5**, 15348, doi:10.1038/srep15348 (2015).
83 Zheng, Q., Jockusch, S., Zhou, Z. & Blanchard, S. C. The contribution of reactive oxygen species to the photobleaching of organic fluorophores. *Photochem Photobiol* **90**, 448-454, doi:10.1111/php.12204 (2014).
84 Magidson, V. & Khodjakov, A. Circumventing photodamage in live-cell microscopy. *Methods in cell biology* **114**, 545-560, doi:10.1016/B978-0-12-407761-4.00023-3 (2013).
85 Khodjakov, A. & Rieder, C. L. Imaging the division process in living tissue culture cells. *Methods* **38**, 2-16, doi:10.1016/j.ymeth.2005.07.007 (2006).
86 Tirlapur, U. K. & Konig, K. Femtosecond near-infrared laser pulse induced strand breaks in mammalian cells. *Cellular and molecular biology* **47 Online Pub**, OL131-134 (2001).
87 Tirlapur, U. K., Konig, K., Peuckert, C., Krieg, R. & Halbhuber, K. J. Femtosecond near-infrared laser pulses elicit generation of reactive oxygen species in mammalian cells leading to apoptosis-like death. *Exp Cell Res* **263**, 88-97, doi:10.1006/excr.2000.5082 (2001).
88 Douthwright, S. & Sluder, G. Live cell imaging: Assessing the phototoxicity of 488 nm and 546 nm light and methods to alleviate it. *Journal of cellular physiology*, doi:10.1002/jcp.25588 (2016).
89 Benrath, J., Zimmermann, M. & Gillardon, F. Substance P and nitric oxide mediate would healing of ultraviolet photodamaged rat skin: evidence for an effect of nitric oxide on keratinocyte proliferation. *Neuroscience letters* **200**, 17-20 (1995).
90 Li, N., Sul, J. Y. & Haydon, P. G. A calcium-induced calcium influx factor, nitric oxide, modulates the refilling of calcium stores in astrocytes. *J Neurosci* **23**, 10302-10310 (2003).
91 Dixit, R. & Cyr, R. Cell damage and reactive oxygen species production induced by fluorescence microscopy: effect on mitosis and guidelines for non-invasive fluorescence microscopy. *Plant J* **36**, 280-290 (2003).
92 Wang, Y. *et al.* Laser stimulation can activate autophagy in HeLa cells. *Applied Physics Letters* **105**, 173703, doi:doi:http://dx.doi.org/10.1063/1.4900937 (2014).

93 Kalyanaraman, B. *et al.* Measuring reactive oxygen and nitrogen species with fluorescent probes: challenges and limitations. *Free radical biology & medicine* **52**, 1-6, doi:10.1016/j.freeradbiomed.2011.09.030 (2012).
94 Tanida, I., Ueno, T. & Kominami, E. LC3 and Autophagy. *Methods in molecular biology* **445**, 77-88, doi:10.1007/978-1-59745-157-4_4 (2008).
95 Ziolkowska, B., Wozniak, M. & Ziolkowski, P. Co-expression of autophagic markers following photodynamic therapy in SW620 human colon adenocarcinoma cells. *Molecular medicine reports* **14**, 2548-2554, doi:10.3892/mmr.2016.5541 (2016).
96 Miller, D. L. & Korenbrot, J. I. Kinetics of light-dependent Ca fluxes across the plasma membrane of rod outer segments. A dynamic model of the regulation of the cytoplasmic Ca concentration. *The Journal of general physiology* **90**, 397-425 (1987).
97 Yau, K. W. & Nakatani, K. Light-induced reduction of cytoplasmic free calcium in retinal rod outer segment. *Nature* **313**, 579-582 (1985).
98 Neuhaus, G., Bowler, C., Kern, R. & Chua, N. H. Calcium/calmodulin-dependent and -independent phytochrome signal transduction pathways. *Cell* **73**, 937-952 (1993).
99 Hopt, A. & Neher, E. Highly nonlinear photodamage in two-photon fluorescence microscopy. *Biophys J* **80**, 2029-2036, doi:10.1016/S0006-3495(01)76173-5 (2001).
100 Ando, J., Smith, N. I., Fujita, K. & Kawata, S. Photogeneration of membrane potential hyperpolarization and depolarization in non-excitable cells. *Eur Biophys J* **38**, 255-262, doi:10.1007/s00249-008-0397-6 (2009).
101 Berridge, M. J., Bootman, M. D. & Roderick, H. L. Calcium signalling: Dynamics, homeostasis and remodelling. *Nat Rev Mol Cell Bio* **4**, 517-529, doi:10.1038/nrm1155 (2003).
102 Martin, V. V., Beierlein, M., Morgan, J. L., Rothe, A. & Gee, K. R. Novel fluo-4 analogs for fluorescent calcium measurements. *Cell Calcium* **36**, 509-514, doi:10.1016/j.ceca.2004.05.002 (2004).
103 Perez-Terzic, C., Stehno-Bittel, L. & Clapham, D. E. Nucleoplasmic and cytoplasmic differences in the fluorescence properties of the calcium indicator Fluo-3. *Cell Calcium* **21**, 275-282 (1997).
104 Rivas-Sendra, A., Calabuig-Serna, A. & Segui-Simarro, J. M. Dynamics of Calcium during In vitro Microspore Embryogenesis and In vivo Microspore Development in Brassica napus and Solanum melongena. *Front Plant Sci* **8**, 1177, doi:10.3389/fpls.2017.01177 (2017).
105 Song, L. *et al.* Dual optical recordings for action potentials and calcium handling in induced pluripotent stem cell models of cardiac arrhythmias using genetically encoded fluorescent indicators. *Stem Cells Transl Med* **4**, 468-475, doi:10.5966/sctm.2014-0245 (2015).
106 Crocini, C. *et al.* Defects in T-tubular electrical activity underlie local alterations of calcium release in heart failure. *Proc Natl Acad Sci U S A* **111**, 15196-15201, doi:10.1073/pnas.1411557111 (2014).

107 Juillerat, A. *et al.* Directed evolution of O6-alkylguanine-DNA alkyltransferase for efficient labeling of fusion proteins with small molecules in vivo. *Chemistry & biology* **10**, 313-317 (2003).
108 Beharry, A. A., Nagel, Z. D., Samson, L. D. & Kool, E. T. Fluorogenic Real-Time Reporters of DNA Repair by MGMT, a Clinical Predictor of Antitumor Drug Response. *PloS one* **11**, e0152684, doi:10.1371/journal.pone.0152684 (2016).
109 Greenfield, J. J. & High, S. The Sec61 complex is located in both the ER and the ER-Golgi intermediate compartment. *J Cell Sci* **112 (Pt 10)**, 1477-1486 (1999).
110 Liu, W. C. *et al.* Ionomycin, a new polyether antibiotic. *The Journal of antibiotics* **31**, 815-819 (1978).
111 Liu, C. & Hermann, T. E. Characterization of ionomycin as a calcium ionophore. *J Biol Chem* **253**, 5892-5894 (1978).
112 Dedkova, E. N., Sigova, A. A. & Zinchenko, V. P. Mechanism of action of calcium ionophores on intact cells: ionophore-resistant cells. *Membrane & cell biology* **13**, 357-368 (2000).
113 Blau, L. & Weissmann, G. Transmembrane calcium movements mediated by ionomycin and phosphatidate in liposomes with Fura 2 entrapped. *Biochemistry* **27**, 5661-5666 (1988).
114 Rogers, T. B., Inesi, G., Wade, R. & Lederer, W. J. Use of thapsigargin to study Ca2+ homeostasis in cardiac cells. *Bioscience reports* **15**, 341-349 (1995).
115 Andersen, T. B., Lopez, C. Q., Manczak, T., Martinez, K. & Simonsen, H. T. Thapsigargin--from Thapsia L. to mipsagargin. *Molecules* **20**, 6113-6127, doi:10.3390/molecules20046113 (2015).
116 Tsai, F. C. *et al.* A polarized Ca2+, diacylglycerol and STIM1 signalling system regulates directed cell migration. *Nat Cell Biol* **16**, 133-144, doi:10.1038/ncb2906 (2014).
117 Thastrup, O., Foder, B. & Scharff, O. The Calcium Mobilizing and Tumor Promoting Agent, Thapsigargin Elevates the Platelet Cytoplasmic Free Calcium-Concentration to a Higher Steady-State Level - a Possible Mechanism of Action for the Tumor Promotion. *Biochem Bioph Res Co* **142**, 654-660, doi:Doi 10.1016/0006-291x(87)91464-1 (1987).
118 Jackson, T. R., Patterson, S. I., Thastrup, O. & Hanley, M. R. A Novel Tumor Promoter, Thapsigargin, Transiently Increases Cytoplasmic Free Ca-2+ without Generation of Inositol Phosphates in Ng115-401l Neuronal Cells. *Biochemical Journal* **253**, 81-86 (1988).
119 Samanta, K., Bakowski, D. & Parekh, A. B. Key role for store-operated Ca2+ channels in activating gene expression in human airway bronchial epithelial cells. *PloS one* **9**, e105586, doi:10.1371/journal.pone.0105586 (2014).
120 Hom, J. R., Gewandter, J. S., Michael, L., Sheu, S. S. & Yoon, Y. Thapsigargin induces biphasic fragmentation of mitochondria through calcium-mediated mitochondrial fission and apoptosis. *Journal of cellular physiology* **212**, 498-508, doi:10.1002/jcp.21051 (2007).
121 Jiang, S., Chow, S. C., Nicotera, P. & Orrenius, S. Intracellular Ca2+ Signals Activate Apoptosis in Thymocytes - Studies Using the Ca2+-Atpase Inhibitor

Thapsigargin. *Experimental Cell Research* **212**, 84-92, doi:DOI 10.1006/excr.1994.1121 (1994).
122 Furuya, Y., Lundmo, P., Short, A. D., Gill, D. L. & Isaacs, J. T. The Role of Calcium, Ph, and Cell-Proliferation in the Programmed (Apoptotic) Death of Androgen-Independent Prostatic-Cancer Cells Induced by Thapsigargin. *Cancer Res* **54**, 6167-6175 (1994).
123 Neft, N. & Farley, T. M. Conditions influencing antimycin production by a Streptomyces species grown in chemically defined medium. *Antimicrobial agents and chemotherapy* **1**, 274-276 (1972).
124 Quinlan, C. L., Gerencser, A. A., Treberg, J. R. & Brand, M. D. The mechanism of superoxide production by the antimycin-inhibited mitochondrial Q-cycle. *J Biol Chem* **286**, 31361-31372, doi:10.1074/jbc.M111.267898 (2011).
125 Jeong, J. I., Lee, Y. W. & Kim, Y. K. Chemical hypoxia-induced cell death in human glioma cells: role of reactive oxygen species, ATP depletion, mitochondrial damage and Ca2+. *Neurochemical research* **28**, 1201-1211 (2003).
126 Harriman, J. F., Liu, X. L., Aleo, M. D., Machaca, K. & Schnellmann, R. G. Endoplasmic reticulum Ca2+ signaling and calpains mediate renal cell death. *Cell Death Differ* **9**, 734-741, doi:10.1038/sj.cdd.4401029 (2002).
127 Laissue, P. P., Alghamdi, R. A., Tomancak, P., Reynaud, E. G. & Shroff, H. Assessing phototoxicity in live fluorescence imaging. *Nat Methods* **14**, 657-661, doi:10.1038/nmeth.4344 (2017).
128 Donnert, G., Eggeling, C. & Hell, S. W. Major signal increase in fluorescence microscopy through dark-state relaxation. *Nat Methods* **4**, 81-86, doi:10.1038/nmeth986 (2007).
129 Tinevez, J. Y. *et al.* A quantitative method for measuring phototoxicity of a live cell imaging microscope. *Methods in enzymology* **506**, 291-309, doi:10.1016/B978-0-12-391856-7.00039-1 (2012).
130 Sandberg, S., Glette, J., Hopen, G., Solberg, C. O. & Romslo, I. Porphyrin-induced photodamage to isolated human neutrophils. *Photochem Photobiol* **34**, 471-475 (1981).
131 Sandberg, S. & Romslo, I. Porphyrin-induced photodamage at the cellular and the subcellular level as related to the solubility of the porphyrin. *Clinica chimica acta; international journal of clinical chemistry* **109**, 193-201 (1981).
132 Kessel, D. Photodynamic therapy and neoplastic disease. *Oncology research* **4**, 219-225 (1992).
133 Cheng, L. Y. & Packer, L. Photodamage to hepatocytes by visible light. *FEBS letters* **97**, 124-128 (1979).
134 Schneckenburger, H. *et al.* Light exposure and cell viability in fluorescence microscopy. *Journal of microscopy* **245**, 311-318, doi:10.1111/j.1365-2818.2011.03576.x (2012).
135 Birben, E., Sahiner, U. M., Sackesen, C., Erzurum, S. & Kalayci, O. Oxidative stress and antioxidant defense. *The World Allergy Organization journal* **5**, 9-19, doi:10.1097/WOX.0b013e3182439613 (2012).
136 Jena, N. R. DNA damage by reactive species: Mechanisms, mutation and repair. *Journal of biosciences* **37**, 503-517 (2012).

137 Rosenstock, T. R., Carvalho, A. C., Jurkiewicz, A., Frussa-Filho, R. & Smaili, S. S. Mitochondrial calcium, oxidative stress and apoptosis in a neurodegenerative disease model induced by 3-nitropropionic acid. *Journal of neurochemistry* **88**, 1220-1228 (2004).
138 Hamad, I., Arda, N., Pekmez, M., Karaer, S. & Temizkan, G. Intracellular scavenging activity of Trolox (6-hydroxy-2,5,7,8-tetramethylchromane-2-carboxylic acid) in the fission yeast, Schizosaccharomyces pombe. *Journal of natural science, biology, and medicine* **1**, 16-21, doi:10.4103/0976-9668.71667 (2010).
139 Lee, J. H. *et al.* Trolox inhibits osteolytic bone metastasis of breast cancer through both PGE2-dependent and independent mechanisms. *Biochemical pharmacology* **91**, 51-60, doi:10.1016/j.bcp.2014.06.005 (2014).
140 Messier, E. M. *et al.* Trolox contributes to Nrf2-mediated protection of human and murine primary alveolar type II cells from injury by cigarette smoke. *Cell death & disease* **4**, e573, doi:10.1038/cddis.2013.96 (2013).
141 Luo, Y., Chang, C. K. & Kessel, D. Rapid initiation of apoptosis by photodynamic therapy. *Photochem Photobiol* **63**, 528-534, doi:DOI 10.1111/j.1751-1097.1996.tb03079.x (1996).
142 Kessel, D. & Luo, Y. Delayed oxidative photodamage induced by photodynamic therapy. *Photochem Photobiol* **64**, 601-604, doi:DOI 10.1111/j.1751-1097.1996.tb03111.x (1996).
143 Carcamo, J. M. *et al.* Vitamin C is a kinase inhibitor: dehydroascorbic acid inhibits IkappaBalpha kinase beta. *Molecular and cellular biology* **24**, 6645-6652, doi:10.1128/MCB.24.15.6645-6652.2004 (2004).
144 Carcamo, J. M., Borquez-Ojeda, O. & Golde, D. W. Vitamin C inhibits granulocyte macrophage-colony-stimulating factor-induced signaling pathways. *Blood* **99**, 3205-3212 (2002).
145 Bethge, P., Chereau, R., Avignone, E., Marsicano, G. & Nagerl, U. V. Two-photon excitation STED microscopy in two colors in acute brain slices. *Biophys J* **104**, 778-785, doi:10.1016/j.bpj.2012.12.054 (2013).
146 Wang, Y., Maharana, S., Wang, M. D. & Shivashankar, G. V. Super-resolution microscopy reveals decondensed chromatin structure at transcription sites. *Sci Rep* **4**, 4477, doi:10.1038/srep04477 (2014).
147 Kasper, R. *et al.* Single-molecule STED microscopy with photostable organic fluorophores. *Small* **6**, 1379-1384, doi:10.1002/smll.201000203 (2010).
148 Chatterjee, P. K. *et al.* Tempol, a membrane-permeable radical scavenger, reduces oxidant stress-mediated renal dysfunction and injury in the rat. *Kidney international* **58**, 658-673, doi:10.1046/j.1523-1755.2000.00212.x (2000).
149 Wilcox, C. S. & Pearlman, A. Chemistry and antihypertensive effects of tempol and other nitroxides. *Pharmacological reviews* **60**, 418-469, doi:10.1124/pr.108.000240 (2008).
150 DeJong, R. J. *et al.* Reactive oxygen species detoxification by catalase is a major determinant of fecundity in the mosquito Anopheles gambiae. *Proc Natl Acad Sci U S A* **104**, 2121-2126, doi:10.1073/pnas.0608407104 (2007).

151 Distelmaier, F. *et al.* Trolox-sensitive reactive oxygen species regulate mitochondrial morphology, oxidative phosphorylation and cytosolic calcium handling in healthy cells. *Antioxidants & redox signaling* **17**, 1657-1669, doi:10.1089/ars.2011.4294 (2012).
152 Oracz, J., Westphal, V., Radzewicz, C., Sahl, S. J. & Hell, S. W. Photobleaching in STED nanoscopy and its dependence on the photon flux applied for reversible silencing of the fluorophore. *Sci Rep* **7**, 11354, doi:10.1038/s41598-017-09902-x (2017).
153 Wu, Y. *et al.* Resonant Scanning with Large Field of View Reduces Photobleaching and Enhances Fluorescence Yield in STED Microscopy. *Sci Rep* **5**, 14766, doi:10.1038/srep14766 (2015).
154 Schneider, J. *et al.* Ultrafast, temporally stochastic STED nanoscopy of millisecond dynamics. *Nat Methods* **12**, 827-830, doi:10.1038/nmeth.3481 (2015).
155 Donnert, G., Eggeling, C. & Hell, S. W. Triplet-relaxation microscopy with bunched pulsed excitation. *Photochemical & photobiological sciences : Official journal of the European Photochemistry Association and the European Society for Photobiology* **8**, 481-485, doi:10.1039/b903357m (2009).
156 Szalay, G. *et al.* Fast 3D Imaging of Spine, Dendritic, and Neuronal Assemblies in Behaving Animals. *Neuron* **92**, 723-738, doi:10.1016/j.neuron.2016.10.002 (2016).
157 Bullen, A. & Saggau, P. High-speed, random-access fluorescence microscopy: II. Fast quantitative measurements with voltage-sensitive dyes. *Biophys J* **76**, 2272-2287, doi:10.1016/S0006-3495(99)77383-2 (1999).
158 Court, N. W., Ingley, E., Klinken, S. P. & Bogoyevitch, M. A. Outer membrane protein 25-a mitochondrial anchor and inhibitor of stress-activated protein kinase-3. *Biochim Biophys Acta* **1744**, 68-75, doi:10.1016/j.bbamcr.2004.11.008 (2005).
159 Velasco, A. *et al.* Cell type-dependent variations in the subcellular distribution of alpha-mannosidase I and II. *J Cell Biol* **122**, 39-51 (1993).
160 Biterge, B. & Schneider, R. Histone variants: key players of chromatin. *Cell and tissue research* **356**, 457-466, doi:10.1007/s00441-014-1862-4 (2014).
161 Fiszer-Kierzkowska, A. *et al.* Liposome-based DNA carriers may induce cellular stress response and change gene expression pattern in transfected cells. *Bmc Mol Biol* **12**, 27 doi: 10.1186/1471-2199-12-27 (2011).
162 Bottanelli, F. *et al.* A novel physiological role for ARF1 in the formation of bidirectional tubules from the Golgi. *Molecular biology of the cell* **28**, 1676-1687, doi:10.1091/mbc.E16-12-0863 (2017).
163 Rankin, B. R. *et al.* Nanoscopy in a living multicellular organism expressing GFP. *Biophys J* **100**, L63-65, doi:10.1016/j.bpj.2011.05.020 (2011).